

The winds of OBA hypergiants and luminous blue variables

Dynamically-consistent atmosphere models reveal multiple wind regimes

M. Bernini-Peron¹, A.A.C. Sander^{1,2}, G.N. Sabhahit³, F. Najarro⁴, V. Ramachandran¹, and J.S. Vink³

¹ Zentrum für Astronomie der Universität Heidelberg, Astronomisches Rechen-Institut, Mönchhofstr. 12-14, 69120 Heidelberg
e-mail: matheus.bernini@uni-heidelberg.de

² Interdisziplinäres Zentrum für Wissenschaftliches Rechnen, Universität Heidelberg, Im Neuenheimer Feld 225, 69120 Heidelberg, Germany

³ Armagh Observatory and Planetarium, College Hill, Armagh BT61 9DG, N. Ireland

⁴ Departamento de Astrofísica, Centro de Astrobiología, (CSIC-INTA), Ctra. Torrejón a Ajalvir, km 4, 28850 Torrejón de Ardoz, Madrid, Spain

Received December 23, 2025; accepted XXXXXXXX XX, XXXX

ABSTRACT

Context. OBA hypergiants are evolved massive stars with notable wind features in their optical spectrum. Located at the cool end of the line-driven wind regime, many of these objects are candidate luminous blue variables (LBVs) and presumably close to the Eddington Limit. Despite representing a rather short-lived stage in the life of massive stars, they strongly impact their surroundings and subsequent stellar evolution via their high wind mass loss.

Aims. We aim to investigate the atmospheric conditions and mechanisms that produce the winds and spectral appearance of hypergiants across the OBA temperature regime, thereby covering also typical temperatures of minimum and maximum phases of non-eruptive LBVs.

Methods. We use the hydrodynamically-consistent version of the PoWR atmosphere code to produce a sequence of atmosphere models with a classical Eddington parameter $\Gamma_e \sim 0.4$ and moderate turbulent pressure, in line with typical parameters obtained in the regime of cool supergiants and hypergiants. We vary the inner boundary effective temperature from ~ 12.5 kK to ~ 38.0 kK. Our main model series is calculated at solar metallicity, with a few additional tests performed at lower metallicity.

Results. We find a complex pattern of the mass-loss rate as a function of temperature across the hypergiant regime with regions of higher and lower rates associated with different types of wind solutions, which we name as “dense” and “airy”. We find known hypergiants and LBVs with spectra resembling the synthetic spectra of our models for all of the wind-solution regions. Around the temperatures where Fe IV recombines to Fe III and Fe III recombines to Fe II, we find a bi-stability of solutions and sharp increases in the mass-loss rate. In addition, we find “drops” when the leading Fe ion is changing at the wind onset, indicating that wind solutions switch from dense to airy in case of insufficient driving opacity. The resulting velocity fields in the different regions reflect the different atmosphere solutions, where the airy solutions align with the empirical relation between terminal velocity and effective temperature.

Conclusions. Our results demonstrate the existence of the first and second bi-stability jump and their association with Fe recombination in the hypergiant regime. However, the jumps are embedded in an overall more complex behavior that does not well align with any existing mass-loss recipe. Towards cooler temperatures, the role of turbulent pressure in the wind acceleration becomes increasingly important, in particular in the airy regimes. Combining our results with other recent modelling efforts, we suggest that the switch between airy and dense regimes only happens within a certain proximity to the Eddington Limit, while otherwise only either dense or airy solutions will be obtained. Calculations exploring a wider parameter regime and incorporating a more sophisticated treatment of radiatively-driven turbulence will be necessary to further test this hypothesis.

Key words. stars: atmospheres – stars: early-type — stars: mass-loss – stars: supergiants – stars: winds, outflows

1. Introduction

Mass loss is a key ingredient that can shape the entire evolution of a massive star ($M \gtrsim 8 M_\odot$) since its birth as an O/early-B star until their eventual core collapse (see, e.g., Langer 2012; Smith 2014; Vink 2022, for recent reviews). While the post-main-sequence stage represents only $\sim 10\%$ of a star’s lifetime, dramatic changes in the stellar properties, such as surface chemical composition, luminosity, and temperature, can be observed. These changes considerably affect the resulting stellar wind properties such as the mass-loss rate \dot{M} , which in turn is a major ingredient for the subsequent evolution. Therefore, a quantitative understanding of the interplay between the stellar and wind

properties is key to better connect the observed stages of massive post-main-sequence stars and predict their evolutionary fates.

Towards the cool end of the line-driven wind regime, we find late-B and A supergiants and hypergiants¹. Many of these are luminous blue variables (LBVs) or LBV candidates. In its raw definition, the LBV phenomenon as such is not an evolutionary stage, but an observational umbrella term (Conti 1984) that encompasses several different objects and phenomena, namely: eruptive variables (e.g., η Car), P-Cygni supergiants (e.g., P Cyg, HD 316285), and S-Dor variables (e.g., S Dor, MWC 930).

¹ In this work, we use the “hypergiant” definition by Clark et al. (2012) based exclusively on spectral morphology (cf. Negueruela et al. 2024).

This class of objects, which frequently produces nebulae around them, is expected to play a pivotal role in the evolution of massive stars as they are likely the gateway to stages such as WRs and/or core-collapse supernovae (CCSNe), especially of IIn types (e.g. Kotak & Vink 2006; Trundle et al. 2008; Nyholm et al. 2020). Moreover, they are expected to be the second main source of metal enrichment of their host galaxies (e.g., Aglizzo et al. 2021). They are also producers of complex carbon molecules due to their sufficiently high temperatures, high mass-loss rates, and variability – extremely relevant for astrobiology (Arun et al. 2025).

Such a “zoo” of stars spans a wide range of effective temperatures and luminosities ($T_{\text{eff}} = 6 \dots 40 \text{ kK}$; $\log L = 5.0 \dots 6.5$; e.g., Smith et al. 2019). This parameter range encompasses regions where theoretical models traditionally predict a discontinuous behavior in the wind parameters, attributed to also found discontinuities in a bi-stability of solutions found originally by Pauldrach & Puls (1990) in mCAK-modeling efforts for P Cyg. Later, Lamers et al. (1995) found discontinuities in the ratio between the terminal velocity v_{∞} and the effective escape velocity

$$v_{\text{esc},\Gamma} = \sqrt{\frac{2GM_{\star}}{r}} (1 - \Gamma_{\text{e}}) \quad (1)$$

for a sample of OBA supergiants.

Incorporating this discontinuity in $v_{\infty}/v_{\text{esc},\Gamma_{\text{e}}}$, modelling efforts in a broader parameter regime using a Monte Carlo approach (Vink et al. 1999) yielded two particular sharp increases (“jumps”) in the behavior of \dot{M} as a function of decreasing effective temperature T_{eff} : A first one at $T_{\text{eff}} \approx 25 \text{ kK}$, the so-called “first bi-stability jump” (1-BiSJ), which could be traced back to a recombination from Fe IV to Fe III in the atmosphere, and a second one at $T_{\text{eff}} \approx 10 \text{ kK}$, the “second bi-stability jump” (2-BiSJ), attributed to a recombination from Fe III to Fe II. These are also included in the mass-loss description from Vink et al. (2001), which is widely employed in stellar evolution. The jumps have further independently been found of any assumption in $v_{\infty}/v_{\text{esc},\Gamma_{\text{e}}}$ and other methodologies than the Monte Carlo calculations (e.g., Müller & Vink 2008; Vink & Sander 2021). Commonly, only the 1-BiSJ is explicitly incorporated while the switch to the \dot{M} -treatment for cooler stars approximately incorporates the effect of the second one if using a recipe with a high mass loss, such as de Jager et al. (1988).

Concerning the 1-BiSJ, recent multiwavelength quantitative spectroscopic studies on BSGs challenge this scenario (e.g., Bernini-Peron et al. 2023, 2024; Verhamme et al. 2024; Alkousa et al. 2025; de Burgos et al. 2024), not finding signs of increases – at best a rather constant trend, better captured by the \dot{M} prescriptions of Krtička et al. (2024). Moreover, the discontinuity in $v_{\infty}/v_{\text{esc},\Gamma_{\text{e}}}$ is also contested (Crowther et al. 2006; Markova & Puls 2008; Alkousa et al. 2025). However, in the LBV regime

Regarding the 2-BiSJ, the scientific panorama remains very unexplored, both due to the much more sparse UV spectral coverage of late-B and A supergiants and the challenges in modeling this parameter regime. Therefore, there are hardly any investigations dedicated specifically on the wind behavior in this regime. Using a grid of CMFGEN models with global wind consistency, Petrov et al. (2016) found the 2-BiSJ associated with the change in ionization of Fe III to Fe II for models with high luminosity-to-mass ratio (L/M). In that line, Sabhahit et al. (2025), using a grid of fully hydrodynamically consistent models, also found an increase in \dot{M} driven by Fe II for models with high L/M . However, their investigation was motivated by the enhanced \dot{M} of very massive stars and thus their grid in this region is sparse.

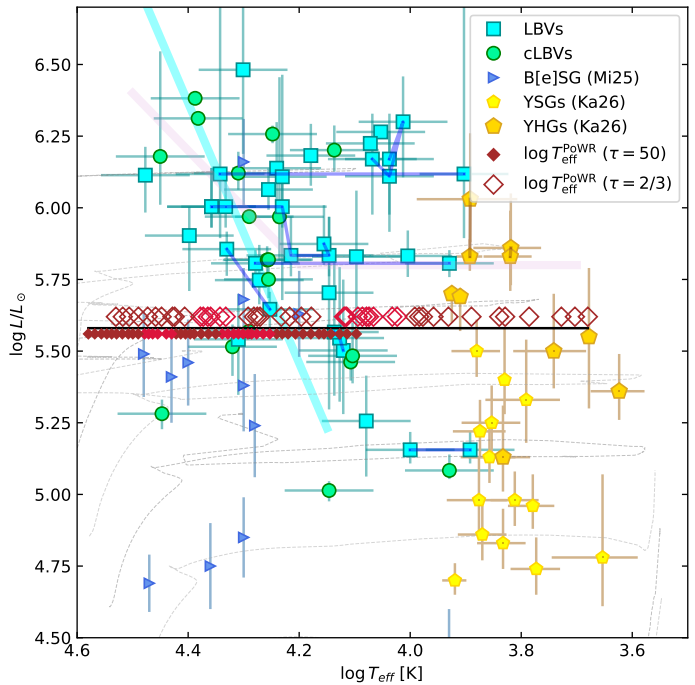


Fig. 1. HR diagram depicting our model sequence against LBVs (cyan squares), B[e]SG (blue triangles), OBA hypergiants/candidates (green circles), YSGs (small yellow pentagons), and YHGs (big gold pentagons) from the literature – see Appendix Sect. F. The luminosities are updated to distances mostly based on Gaia DR3 (Bailer-Jones et al. 2021; Gaia Collaboration et al. 2023). The black line indicates the luminosity of our sequence. The small diamonds below indicate the T_* while the large hollow diamonds indicate the $T_{2/3}$. The thin dotted lines indicate the galactic evolutionary tracks by Ekström et al. (2012). The thick cyan line indicates the LBV instability strip (Groh et al. 2011) and the thick violet line indicates the HD limit (Humphreys & Davidson 1979).

In this work, we use hydrodynamically consistent atmosphere models to show that the mass-loss and other wind properties of stars closer to the Eddington limit in the Hertzsprung Gap region (usually occupied by hypergiants and LBVs) have indeed a complex behavior indeed. This is strongly tied to the interplay of changes in the ionization of Fe, H, and He, as well as to the action of the star’s atmospheric turbulent pressure.

In Sect. 2 we briefly describe the tools, approach, and assumptions. In Sect. 3, we briefly illustrate the resulting optical spectra and their resemblance to known LBVs and BHGs before presenting the obtained trends in mass-loss rate and wind structure. We then discuss implications of our results in Sect. 4 before eventually drawing the conclusions in Sect. 5.

2. Methods

We use the PoWR^{HD} (Sander et al. 2018) stellar atmosphere code to produce a fine-spaced sequence of hydrodynamically consistent models of massive stars with moderate mass and luminosity, but still close to the Eddington Limit. We select the option to fix all stellar parameters to have PoWR^{HD} computing the velocity field (incl. v_{∞}) and \dot{M} .

We fix the mass ($20.6 M_{\odot}$), luminosity ($\log L/L_{\odot} = 5.58$), and a mild enriched He abundance (with He mass fraction $X_{\text{He}} = 0.33$) as well as the same CNO composition from Bernini-Peron et al. (2025). Motivated by time-dependent hydrodynamical simulations of Driesen et al. (2019), who found that stars below

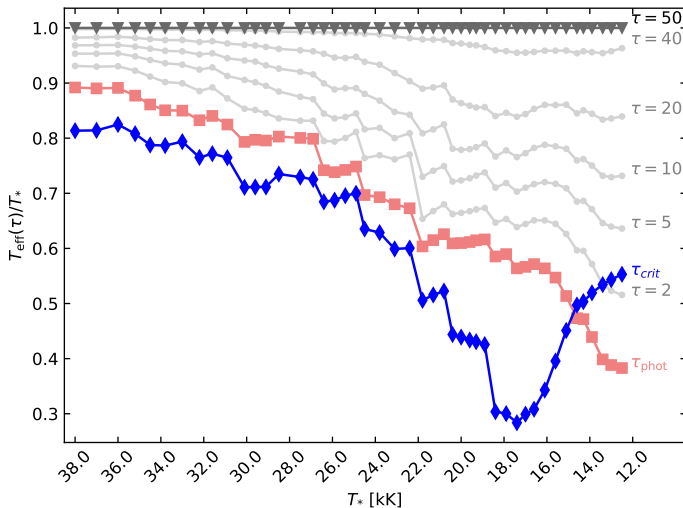


Fig. 2. Effective temperature at different optical depths τ , normalized by $T_{\star} = T_{\text{eff}}(\tau = 50)$ for each point of the sequence. The pink curve indicates the $T_{2/3}$ and the blue curve indicates the T_{eff} at the critical point.

$T_{\text{eff}} < 20$ kK have lower clumping, we fix the volume filling factor $f_{\text{vol}} = 0.33$ at all depth points.

We adopt a depth-independent turbulence velocity ($v_{\text{turb}} = 20$ km s $^{-1}$), as typically employed in atmospheres of LBVs and even some BSGs/BHGs (e.g., Groh et al. 2009). However, we note that this value might be an underestimation, especially for the hotter models of our sequence, as recent multi-D simulations of atmospheres for stars with high $\Gamma_e(R_{\text{crit}})$ (Moens et al. 2025) predict much higher values of $v_{\text{turb}} \sim 150$. Yet, as we aimed for a homogeneous sequence of models isolating the effect of a T_{\star} variation, we keep v_{∞} (and other parameters) fixed.

Concerning the atomic physics, we consider the elements H, He, C, N, O, Si, S, Al, P, Mg, and the iron-group elements (G) – which, albeit largely dominated by Fe, conflates levels and transitions from Sc to Ni. In Appendix Sect. A we disclose the considered levels and transitions for each element.

In our main model sequence, we vary only the temperature at the inner boundary $T_{\star} = T_{\text{eff}}(\tau = 50)$, where τ is the Rosseland continuum optical depth, from 13 kK to 38 kK. The photospheric temperature – i.e., $T_{\text{eff}}(\tau = 2/3)$, hereafter simply $T_{2/3}$ – is an output quantity that depends on the resulting \dot{M} . As our model sequence has high Γ_e values, their atmospheres are expanded, such that the difference between T_{\star} and $T_{2/3}$ amounts to ~ 7 kK. In Fig. 1, we show the location of our model sequence, indicating both T_{\star} and $T_{2/3}$, in the Hertzsprung–Russell diagram (HRD) together with a set of known objects in the hypergiant and LBV domain. All comparison data is taken from the literature, though the luminosities have been updated where newer distance information from Gaia DR3 is available – see Appendix Sect. F.

A more direct illustration of the difference between T_{\star} and $T_{2/3}$ at different optical depth is shown in Fig. 2. Despite some scatter on small scales, it is clear that the atmospheres get more extended with cooler T_{\star} and the difference between T_{\star} and $T_{\text{eff}}(\tau < 50)$ increases. For the coolest models, the effective temperature of the critical point becomes smaller than $T_{2/3} = T_{\text{eff}}(\tau = 2/3)$, meaning the wind stars to launch beneath the layers forming the continuum. This is a signature of an optically thick wind and is known in particular from models describing classical Wolf-Rayet stars (e.g., Sander et al. 2020, 2023; Lefever et al. 2023, 2026).

3. Results

3.1. Spectral appearance

Our PoWR^{HD} models are not specifically designed to fit any particular star and have a fixed luminosity. However, as illustrated in Fig. 3, we find that the normalized synthetic spectra of our models generally resemble spectra of existing hypergiants and LBVs across their temperature domain. This indicates that many hypergiants/LBVs (and even some supergiants), which spectroscopically appear very different from each other, might belong to such L/M regime. Moreover, this is an important “sanity check” for the robustness of the atmospheres’ structures and indicates that our sequence is apprehending their physics across the hypergiant regime.

3.2. The behavior of the mass-loss rate

As we illustrate in Figs. 4 and 5, we find a complex pattern for the derived mass-loss rate as a function of T_{\star} . When considering the “transformed radius”

$$R_t = R_{\star} \left(\frac{v_{\infty}}{\dot{M} \sqrt{f_{\text{cl}}}} \cdot \frac{10^{-4} M_{\odot} \text{yr}^{-1}}{2500 \text{km s}^{-1}} \right)^{2/3}, \quad (2)$$

two main types of wind solutions can be identified: “dense-wind” solutions with $R_t > 200 R_{\odot}$ and “airy-wind” solutions² with smaller R_t (cf. Fig. 4). Significant jumps to higher \dot{M} appear around the temperatures associated with the traditional bistability jumps, but these jumps are not the only abrupt transitions. Instead, we see a more complex pattern as shown in Fig. 5 containing both jumps to higher as well as drops to lower \dot{M} . In the following, we refer to these as “valleys” in $\dot{M}(T_{\star})$.

In the background of Fig. 5, we show a stacked area plot indicating the contributions to the total outward pushing forces

$$\Gamma_{\text{wind}} := \Gamma_{\text{rad}} + \Gamma_{\text{press}} \quad (3)$$

at the critical point R_{crit} with Γ_{rad} summarizing the radiative line and continuum accelerations while Γ_{press} includes the acceleration due to gas and turbulent pressure gradients, all normalized to gravity g . For the temperatures associated with the two classical BiSJs, we see a clear association with the change in the ionization of Fe. However, the other end of the valleys, i.e., the decline of \dot{M} down to the low values before the jumps, is less abrupt and seem to be associated with the gradual increase in contribution of other elements and the pressure term. This, in turn, seems indirectly caused by a slow transition of the dominance of different Fe ions. A similar behavior was recently mapped for stars close to the Eddington limit (Lefever et al. 2025; Sabhahit et al. 2025) but pertaining to a much higher luminosity regime.

A further inspection of the relative contributions to Γ_{wind} in Fig. 5 shows that radiatively driven processes dominate the wind acceleration. However, the sheer proximity to the Eddington Limit of the model sequence ($\Gamma_e \approx 0.4$) leads to the effect that in all models less than half of the acceleration at the critical point is actually provided by line opacities. Beside a large contribution from free-electron (i.e., Thomson) scattering, also the continuum opacity of hydrogen as well as acceleration due to gas and turbulent pressure gradients need to be taken into account. In the following, we will discuss the different features in

² We do not label them as “thick” and “thin” as they do not coincide with the wind-optical depth τ_{F} crossing unity. The thick solutions have a higher τ_{F} , but there is no uniform transition value among the sequence.

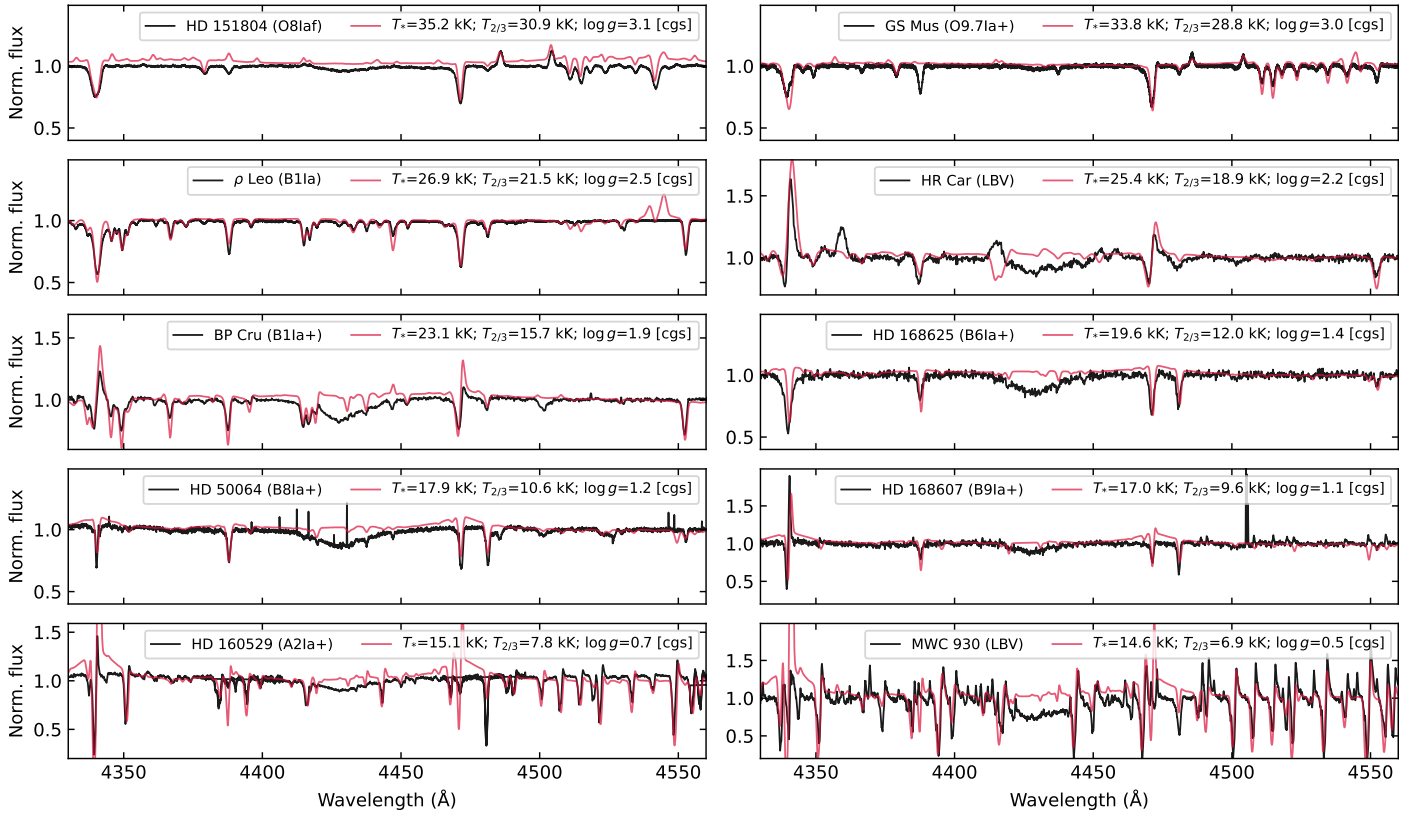


Fig. 3. Non-tailored comparison between the output spectra of some of the models (red lines) and observed spectra (black lines) of OB supergiants/hypergiants and LBVs.

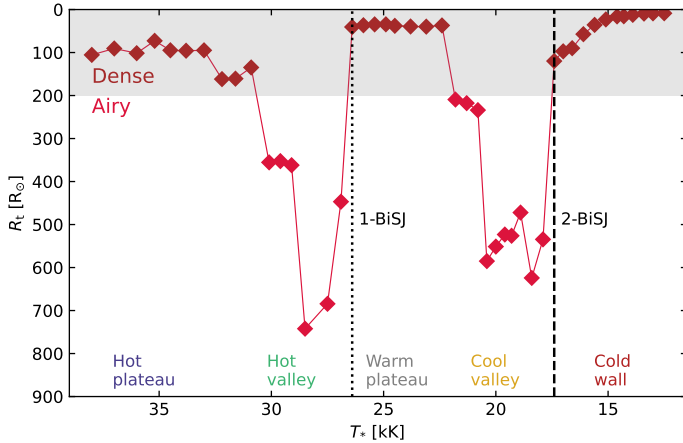


Fig. 4. Transformed radius (R_t) versus T_* : Model with $R_t < 200 R_\odot$ are in the “dense” wind regime – i.e., with higher \dot{M} and optical spectra crowded with emission/P Cygni features – (shaded region). The colored texts in the lower part of the diagram name the wind-solution regions identified in the T_* sequence. The 1-BiSJ and the 2-BiSJ are indicated by the dotted and dashed lines in the transitions from a valley to a plateau (i.e., increase in \dot{M}) when moving towards lower T_* .

the mass-loss trend and consider, for this, also the work ratios

$$Q_k = \int_{R_*}^{\infty} a_{\text{rad},k} dr / \int_{R_*}^{\infty} \left(v \frac{dv}{dr} + \frac{GM_*}{r^2} \right) dr, \quad (4)$$

where the $a_{\text{rad},k}$ is the radiative acceleration due to the respective contribution k (e.g., electron scattering, gas pressure, Fe, H, CNO, etc). In Fig. 6, we plot both $\Gamma_e(r_{\text{crit}})$ as well as Q_e , finding that the valleys in \dot{M} match with regions of low Q_e , i.e., a

low global contribution of the electron scattering and thus a high amount of line driving.

The hot dense-wind plateau: The hottest models in the sequence have moderately high $\log \dot{M} \sim -6$ and probe the temperature range of OHGs. The winds in this region are largely Γ_e - and Fe IV-driven. Pressure and other elements contribute up to $\sim 25\%$ to launch the wind.

The obtained terminal velocities match the v_∞ determined by Prinja et al. (1990) for GS Mus (O9.7Ia+, Carretero-Castrillo et al. 2023), one of the few galactic OHG that has a UV spectrum. The $T_{2/3}$ and $\log g(\tau = 2/3)$ also match the results obtained by Holgado et al. (2020), which results in a very similar spectral appearance. We also find a similar spectral appearance of HD 151804 (formally a O8Iaf) in the optical. In the UV we find a seemingly slow wind. It is possible that elements like Ar, which is shown to influence v_∞ in earlier O stars and not included in our sequence, may start playing a role. While not performing a dedicated spectral analysis, we scale the flux of our models to the observed SED (see appendix Sect. D) to determine the luminosities of GS Mus and HD 151804 ($\log L/L_\odot \sim 5.2$ and $\log L/L_\odot \sim 6.0$) and place them in the HRD (cf. Fig. 1).

The hot airy-wind valley: As Fe IV slowly loses dominance, the available opacity is insufficient to maintain a deeper wind launching associated with a higher mass-loss rate. With τ_{crit} decreasing, CNO and other metal lines contribute quite significantly to the wind launching, as does the pressure term. In this regime, the winds reach $\sim 1000 \text{ km s}^{-1}$, which resemble winds of BSGs (\sim B1 Ia) on the verge of the predicted classical 1-BiSJ

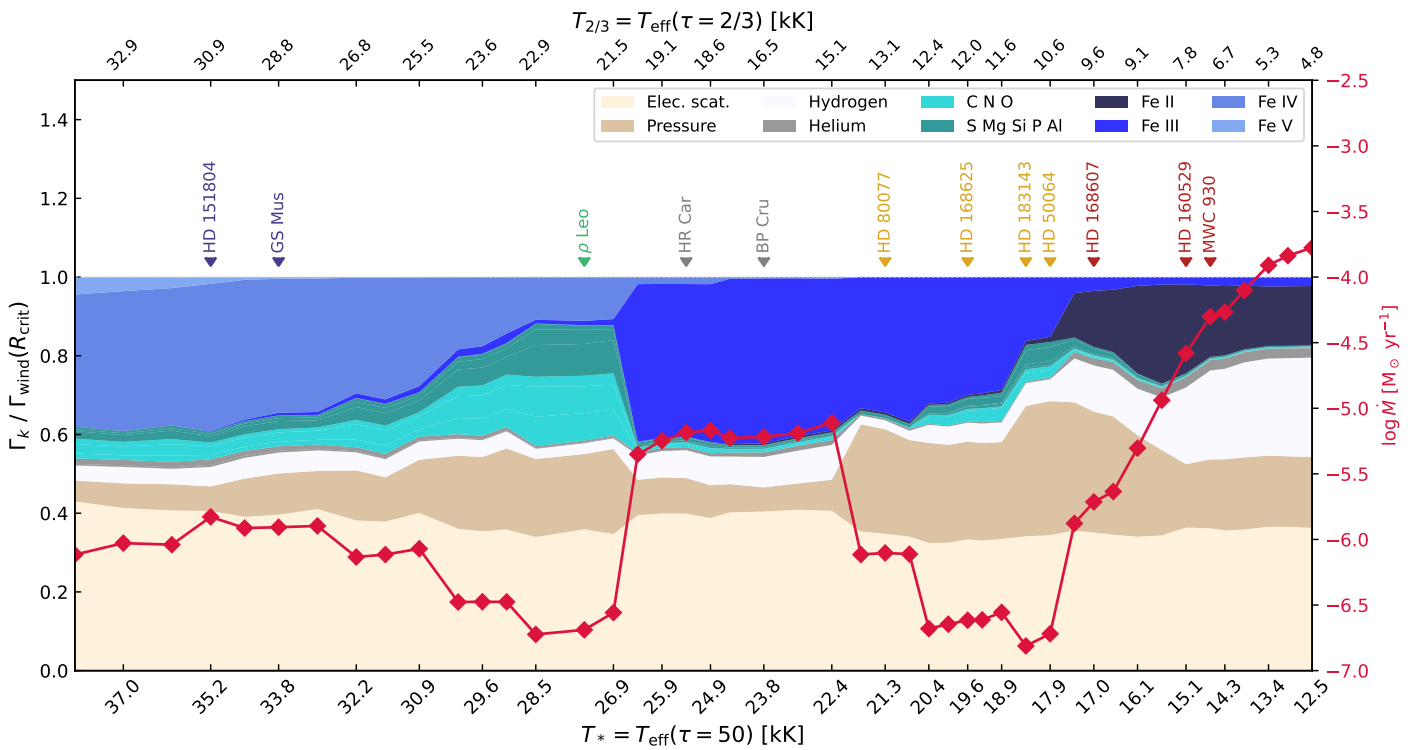


Fig. 5. Contributions of different processes/elements/ions to the wind launching at the critical point (stacked area plot) and corresponding mass-loss rates (red line) for different inner boundary temperatures (T_*). Bottom-up, the light beige area indicate the electron scattering acceleration, the dark beige the pressure, and the smokewhite indicate H₁ continuum driving. The teal tones indicate the contribution of CNO and other metals while the shades of blue indicate the contributions of different Fe ions.

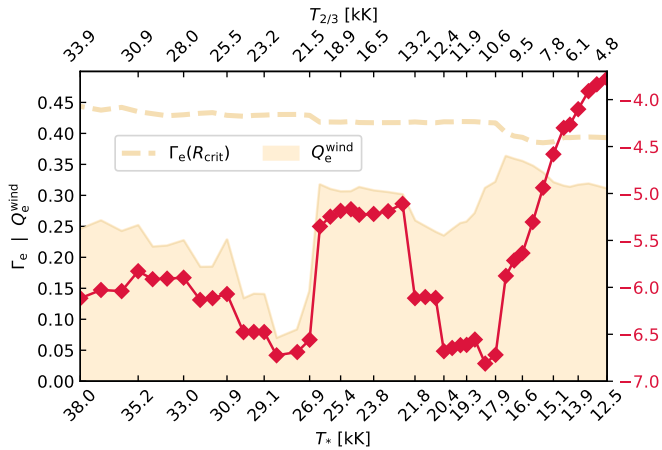


Fig. 6. Comparison between the mass-loss rates trend (red curve) and both the classical Eddington parameter at the critical point $\Gamma_e(R_{\text{crit}})$ (thick dotted curve) and the total contribution of the electron scattering to the work ratio Q_e^{wind} (shaded area).

(Vink et al. 2001). Spectroscopically, we also see a match between models in this range and the B1 Ia supergiant ρ Leo.

The classical first jump and the warm dense-wind plateau:

At $T_* \sim 27$ kK ($T_{2/3} \sim 22$ kK) we see a very sharp increase in \dot{M} which is directly associated with the increase of Fe III contributing to the wind driving. This is the 1-BiSJ already seen in the Monte Carlo models by Vink et al. (1999); Vink & Sander (2021), albeit with shifts in the temperature. In appendix C, we show that we actually find a bi-stability of solutions at this regime transition, but just pick one of them for clarity of

the overall plots such as Fig. 5. Towards cooler temperatures, we then remain in the regime of high \dot{M} until $T_* \sim 23$ kK ($T_{2/3} \sim 15$ kK). Contrary to the Vink et al. (1999) results, we do not find a gradual decrease in \dot{M} after the jump, but occur a plateau. As for the hot plateau before, the contributions beside Fe and Γ_e amount only to $\sim 20\%$.

The atmosphere/wind solution we obtain when in this region is very similar to the solution obtained for the PoWR^{HD} model of ζ^1 Sco (B1.5Ia+ Bernini-Peron et al. 2025). In fact, the corresponding spectra for models in this regime resemble the spectrum of BP Cru (B1Ia+/HMXB), a hypergiant with similar properties to ζ^1 Sco (Clark et al. 2012). We also notice that it resembles the spectrum of HR Car in 2017, suggesting the star is currently in this dense wind regime. At this temperature range we also find LBVs like P Cyg (B1Ia+/LBV), whose spectra are much more extreme, which suggests either a considerably different clumping structure or a higher L/M ratio. In opposition, we also see stars like HD190603 (B1.5Ia+) and ζ^1 Sco, which have less prominent P Cygni features – see Sect. 6.3 in Bernini-Peron et al. (2025) for a discussion on the effects of clumping in the spectra of early-type BHGs.

The cool airy-wind valley At $T_* \sim 22$ kK ($T_{2/3} \sim 15$ kK), we find a drop in the mass-loss rates of more than an order of magnitude. This behavior is the opposite of what was predicted for the classical BiSJ and is not associated with any major changes in the ions (in particular Fe) driving the wind. Nonetheless, the wind solution changes and τ_{crit} decreases again. This happens due to the fact that the Fe III opacities are no longer sufficient to launch the wind at similar radii as obtained for the solutions of the warm dense-wind plateau. Yet, Fe II is not sufficiently populated to take over the wind launching. Instead, the pressure

term supports (quasi-)hydrostatic equilibrium, until an outflow is launched further out, at the expense of a considerably reduced \dot{M} . Unlike the hot airy-wind valley, non-Fe metal lines do not significantly contribute to the wind launching ($\lesssim 10\%$), while the contribution of the pressure term is even stronger.

The synthetic model spectra in this regime resemble the appearance of several late-type BHGs (B2...B9) – e.g., HD80077, HD183143, and HD168625. Notably, a lot of the known BHGs in this temperature regime ($T_{2/3} \sim 14\ldots10$ kK) also display the obtained weak hypergiant characteristics, i.e., $H\beta$, $H\gamma$, $H\delta$, with possibly He and metal lines in P Cygni or emission. In fact, the hypergiant status is questioned for some of those stars as $H\beta$ is variable and often fully in absorption (see Negueruela et al. 2024). Our finding of the cool airy-wind valley indicates that these weaker characteristics could be a natural outcome of the opacity situation in the atmosphere rather than reflecting a lower L/M . This would mean that earlier-type BHGs such as HR Car, BP Cru, or ζ^1 Sco are not necessarily closer to the classical Eddington Limit, but rather have more favorable wind conditions.

The classical second jump and the cold dense-wind wall: Towards even lower temperatures, we find a significant increase in \dot{M} at $T_* \sim 17$ kK ($T_{2/3} = 10$ kK) which is associated with the change from Fe III to Fe II in the wind driving. The higher wind density causes the models' spectra in this regime to resemble AHGs and LBVs that have P Cygni/emission features, such as HD160529 and the LBV MWC 930, crowded with Fe II profiles, in the case of the coolest models. Approximately similar in $T_{2/3}$, this essentially represents the 2-BiSJ predicted by Vink et al. (1999) and Petrov et al. (2016). The jump also occurs in the LBV models by Vink & de Koter (2002), albeit at temperatures more similar to our T_* value. As for the 1-BiSJ, we also find a bi-stability of solutions at the onset of the cold dense-wind wall. We illustrate this further in Appendix C.

Notably, the 2-BiSJ in Petrov et al. (2016) appeared only at the models closer to the classical Eddington limit ($\Gamma_e = 0.39$, $\log L/L_\odot = 5.5$, $M = 20 M_\odot$, $Y = 0.25$), when they transitioned from $T_{2/3} = 10.0$ kK to $T_{2/3} = 8.8$ kK. The jump in their analysis appears in a very similar parameter space and between very similar \dot{M} values (-7.04 to -5.70) than we obtain (-6.7 to -5.8). Interestingly, this similarity in outcome does not coincide with the same driving explanation. Petrov et al. (2016) find that Fe II is responsible for $\sim 70\%$ of the total work ratio, while in our case Fe II contributes only up to $\sim 10\%$ (cf. first panel of Fig. B.1) and most of the contribution comes from electron scattering and pressure. Moreover, when considering the total work ratio Q_{wind} for our models in the cold dense-wind wall, all the Fe ions have a similar contribution. In addition, the total Fe contribution to Q_{wind} is equivalent to that of H and much smaller than that of electron scattering or pressure.

In the models from Petrov et al. (2016), the 2-BiSJ marks the last point of their model sequence. In their models Fe II is not fully recombined at $T_{2/3} = 8.8$ kK, raising the question of the further \dot{M} vs. temperature trend. Our model sequence goes a bit further, and we find that \dot{M} keeps increasing side-by-side with the contribution of Fe II. During the S Doradus cycle, such high values of \dot{M} may explain nebulae around many LBVs and hypergiants – including those which presently do not timely present themselves as bona-fide LBVs. Such a high \dot{M} past the 2-BiSJ may as well explain the signatures of type IIn SNe [e.g.,] (Kotak & Vink 2006; Trundle et al. 2008). Within the capability of our current simulations, we do not reach a stage where the trend in \dot{M} turns over into another plateau or valley. However, we find an

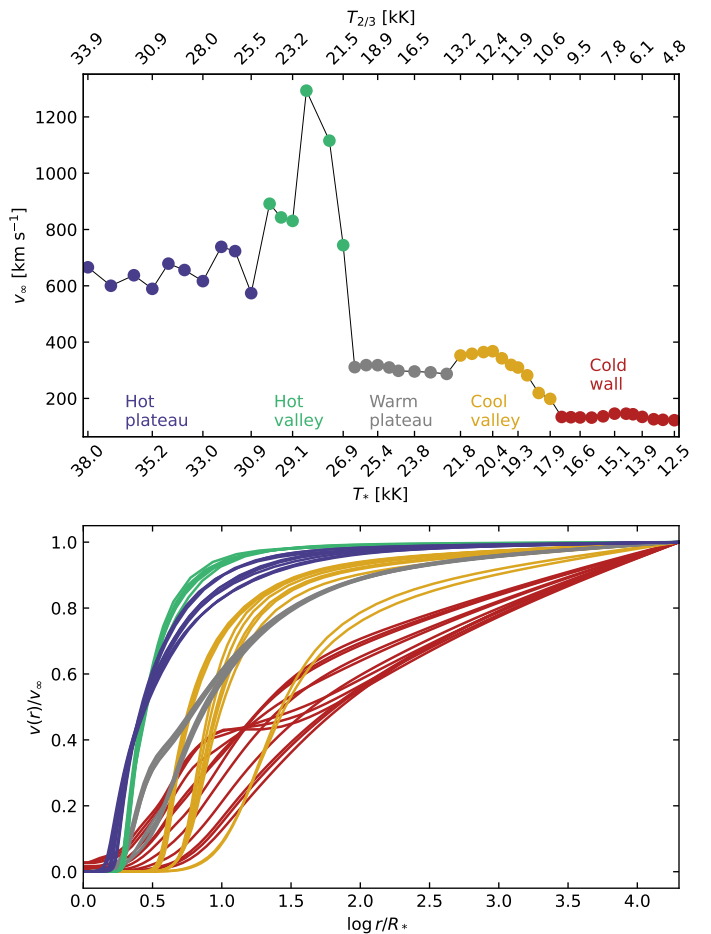


Fig. 7. Terminal velocities (upper panel) and velocity structures (lower panel) of the models along the T_* sequence. Each wind-solution domain is color coded following the scheme of Fig. 4.

indication of a possible stagnation as the increase in \dot{M} becomes smaller for the coolest models in the series which was also suggested by the \dot{M} behavior found by Vink & de Koter (2002).

3.3. Velocity structure

The velocity structures across the temperature sequence reflect the different dense and airy solutions. In the upper panel of Fig. 7 we see that the trends in v trace the five different solution regimes presented above – namely: models in the valleys see an increase in v_∞ compared to models in the plateaus. The differences become even more clear when examining the shapes of $v(r)$, where we see major structural differences for the different solutions (cf. lower panel of Fig. 7). None of the solutions is sufficiently described by a β -velocity law, especially in the wind-launching regime. However, when fitting the solutions of the hot dense-wind plateau (OHG regime, blue curves in Fig. 7) with a single β -law, we obtain solutions resembling the outer wind part with β -values between 1.8 and 2.0, explaining why higher β -values are often favored in traditional analyses of B super- and hypergiants.

The hot dense-wind plateau has $v_\infty \sim 700$ km s⁻¹ and a relatively sharp velocity gradient. At the hot airy-wind valley (BSG-like regime, green curves), we see an increase to ~ 1000 km s⁻¹ and an even more extreme gradient at the critical point. When fitting this regime with β -laws, we obtain slightly higher values of $\beta \approx 2.3$. Crossing the 1-BiSJ into the warm dense-wind plateau (grey curves), we notice a sharp drop in the v_∞ to ~ 300 km s⁻¹.

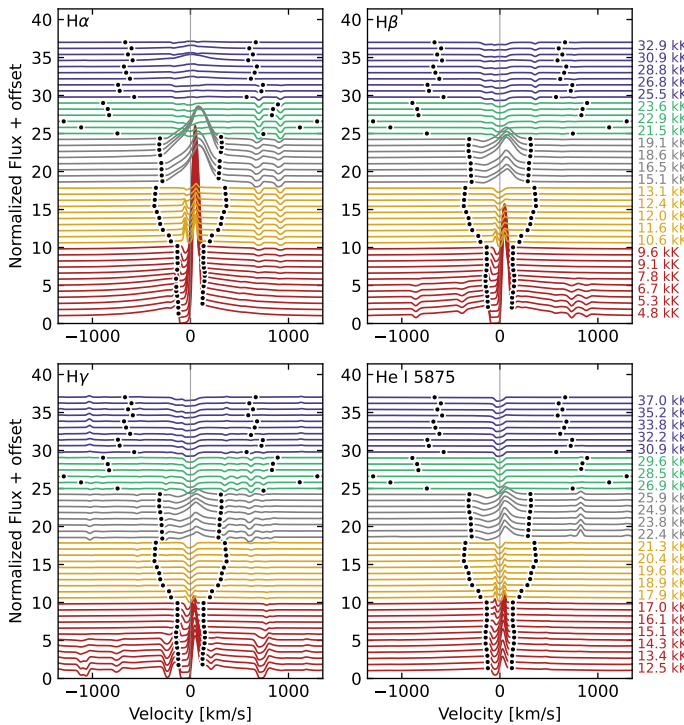


Fig. 8. Hydrogen and Helium profiles in velocity space compared to the terminal velocity (black dots). The color of each spectrum marks to which wind-solution regime the model belongs, following the same colorscheme of Fig. 7. The temperatures rightwards the upper panels indicate the $T_{2/3}$ and rightwards the lower panel indicate the T_{\star} .

In parallel, we also see a noticeable switch in the shapes with a shallower velocity increase and a reduction of the maximum velocity gradient. The corresponding best β -values increase to ~ 4 in this regime, although the representation of the shape in the outer wind clearly shows deviations from a β -law.

Within the cool airy-wind valley (yellow curves), the solutions switch back to a steeper gradient (like in the hot valley previously) but commencing further out in the wind (i.e., larger R_{crit}). The v_{∞} , however, does not increase much relative to the warm plateau while the “best” β increases further to values between 8 and 20. Crossing the 2-BiSJ, in the cold dense-wind wall, we see a rather constant v_{∞} despite a rather sharp increase in the mass-loss rates. This is a consequence of the support by gas and turbulent pressure in the outer wind (see Fig. B.3). As the pressure term drops only with $1/r$, it eventually becomes the dominant in the other wind and is responsible for up to $\sim 50\%$ of the obtained v_{∞} value. This regime cannot be meaningfully described by a β -law any more. Like in the warm plateau, we see important differences in $v(r)$ with the coolest models at $\sim 10R_{\star}$ showing a velocity plateau due to the decreasing influence of Fe II (cf. lowest panel in Fig. B.2).

The different wind regimes and velocity structures also leave their imprint in the resulting synthetic spectra. In Fig. 8, we plot the normalized spectra around the first three Balmer lines as well as He I 5875 Å. In addition, we mark the locations of v_{∞} leftwards and rightwards of the lines’ central wavelength. In the hottest regime as well as in the airy regimes, the lines do not reflect v_{∞} , even if parts are in emission. However, for the warm plateau below the 1-BiSJ, at least H α traces v_{∞} when considering the full emission line width. Below the 2-BiSJ, the P Cygni troughs of all Balmer lines trace well the terminal velocity, while for He I 5875 Å this is only true for the coolest models where He

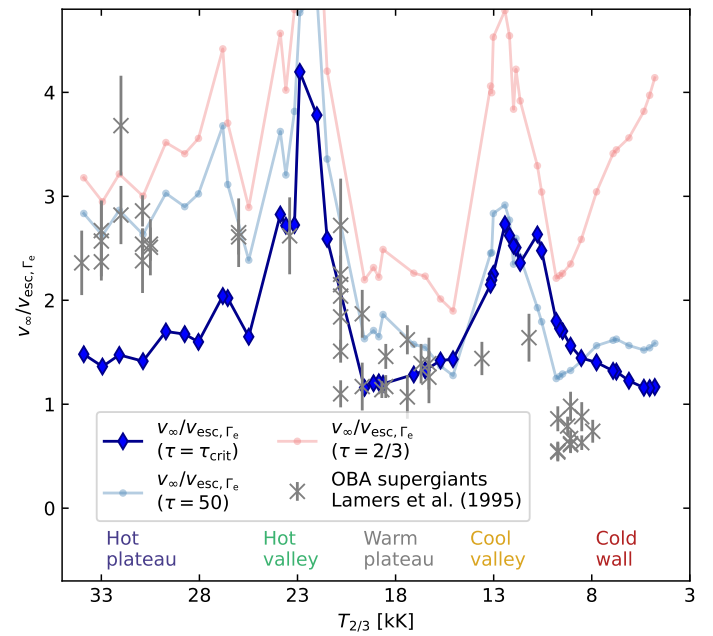


Fig. 9. Behavior of the $v_{\infty}/v_{\text{esc}, \Gamma_e}$ relation. The gray crosses indicate the data of Lamers et al. (1995) for OBA supergiants. The blue curve with diamonds indicates the values for v_{esc, Γ_e} applied to the critical point. The pink curve indicates the ratio at $\tau = 2/3$, and the thin light blue curve indicates the ratio at $\tau = 50$, i.e., the inner boundary.

is totally recombined in the outer atmosphere and can produce the blue absorption.

4. Discussion

4.1. Terminal and escape velocity ratio

From conservation of energy, we expect that the terminal velocity of radiation-driven winds directly depends on $v_{\text{esc}, \Gamma}$ at the stellar surface. For line-driven winds within the mCAK formalism³, $v_{\infty}/v_{\text{esc}, \Gamma} \sim [\alpha/(1-\alpha)]^{1/2}$ where α is the parameter that condenses the blend of optically thin and thick sets of lines (see, e.g. Lamers et al. 1995). This means that changes in the total line opacities – due to, e.g., temperature changes – will affect how v_{∞} and $v_{\text{esc}, \Gamma}$ scale. Using literature values and spectral type calibrations as well as Γ_e estimates based on evolutionary tracks, Lamers et al. (1995) found two jumps in the $v_{\infty}/v_{\text{esc}, \Gamma_e}$ -ratio across the OBA supergiant regime. These were later interpreted as a consequence of changes in the dominant Fe ion (Vink et al. 1999). Newer studies contest the sharpness of these jumps (e.g., Crowther et al. 2006; Markova & Puls 2008).

With our PoWR^{HD} model sequence, we can test the $v_{\infty}/v_{\text{esc}, \Gamma_e}$ -ratio and compare it to Lamers et al. (1995) in Fig. 9. For stars with extended atmospheres, the choice of r in Eq. (1) (where also Γ_e has to be evaluated) is not trivial and we thus plot results for the inner boundary radius (corresponding to $\tau_{\text{Ross,cont}} = 50$), $R_{2/3}$, and the critical radius R_{crit} . As the latter essentially reflects the wind onset, we consider this as the most coherent choice. For models in the hot side of the classical 1-BiSJ, we find that the OBHGs have a lower $v_{\infty}/v_{\text{esc}, \Gamma_e}$ than OBSGs. This is mainly the result of the lower v_{∞} values of the hypergiants, which are at least a factor of two lower than those of comparable supergiants (i.e., similar temperatures). Hence, although Γ_e is higher

³ Modified CAK theory (Castor et al. 1975; Pauldrach et al. 1986).

for hypergiants, the change to $v_{\text{esc},\Gamma}$ resulting from the $\sqrt{1 - \Gamma_e}$ -dependence in Eq. (1) is much smaller.

When entering the hot, airy valley, the terminal velocities become significantly larger due to the lower mass-loss rates. In this regime, some models even exceed the ratio found by Lamers et al. (1995) for BSGs – but in agreement with some results reported in Markova & Puls (2008) –, which is a combined effect of the higher v_∞ and a lower $v_{\text{esc},\Gamma}$ caused by a larger R_{crit} . In the 1-BiSJ regime, where Fe IV recombines to Fe III, the $v_\infty/v_{\text{esc},\Gamma_e}$ -ratio drops sharply to values only slightly above unity, which is in good resemblance with the Lamers et al. (1995) results. While the v_∞ values are very similar to those in the hot valley, the drop in the $v_\infty/v_{\text{esc},\Gamma_e}$ -ratio is mainly caused by the deeper wind launching resulting in lower R_{crit} values (i.e., higher $v_{\text{esc},\Gamma}$).

In the cool valley, before the 2-BiSJ, the ratios increase again. While a glimpse of this might be seen in the results from Lamers et al. (1995), as well as in some of the recent METUJE calculations by Krtička et al. (2025), and possibly also in the empirical determinations by Markova & Puls (2008), we get a much more pronounced effect, again for the same reasons as in the first valley. Crossing the 2-BiSJ, where the Fe III → Fe II switch happens, then coincides with another drop in $v_\infty/v_{\text{esc},\Gamma_e}$, which is also reflected in the data from Lamers et al. (1995), albeit with an offset. However, since the turbulent pressure term influences v_∞ considerably in this regime as discussed above, we might overestimate the ratio by up to a factor of two, which would bring our data in line with Lamers et al. (1995), despite their rough temperature assumptions from spectral types for the B and A stars.

Our $v_\infty/v_{\text{esc},\Gamma_e}$ in the A-star regime are also larger than the values obtained from the so-called “ δ -slow” solutions by Curé et al. (2011) and empirical values listed therein. Again, we attribute this to the influence of the pressure term in the outer wind, which consists of a gas pressure and a turbulent pressure component. In the current framework, both components are treated together as an isotropic pressure. The turbulent pressure is further described with a constant v_{turb} . While the value is clearly motivated by observations (e.g., Searle et al. 2008), multi-dimensional time-dependent hot star atmosphere simulations in the WR- and O-type star domain from Moens et al. (2022) and Debnath et al. (2024) suggest that radiatively-driven turbulence is no longer isotropic in the supersonic wind. While a more detailed treatment of radiatively-driven turbulence requires a major update of the 1D hydrodynamic framework as well as calibration with multi-dimensional models, it is clear that solutions with a leading $1/r$ -acceleration in the outer wind have to be critically reviewed. In the case of the coolest models, Fig. B.3 clearly shows that the turbulent velocity is larger than the sound speed, meaning that the outermost wind solution is dominated by v_{turb} , similar to the models in Sabhahit et al. (2025). These results, as well as the ongoing discussions about turbulent pressure as a driver for cool massive star outflows (e.g., Stothers 2003; Kloczkova 2019; Kee et al. 2021), underline that turbulent pressure is an important ingredient at the cool end of the massive star regime, requiring the development of a more coherent framework addressing the interplay between radiative acceleration and radiatively-driven turbulence in launching mass outflows.

Another caveat when discussing terminal velocities in hydrodynamically-consistent modelling is the choice of wind clumping, which can affect the calculated v_∞ by enhancing opacities. In this work, we fixed $f_{\text{cl}} = 3$ throughout the whole sequence to a value motivated for the BSG regime by the line-deshadowing instability simulations from Driessen et al. (2019). As discussed in their work and also empirically supported, the clumping in the supersonic region in early-B/O supergiants (i.e.,

on the hot side of the 1-BiSJ) are expected to be much larger ($f_{\text{cl}} \sim 20$) than later-type BSGs. Therefore, it is plausible that v_∞ is systematically underestimated for the hottest models of our sequence (i.e., in the hot plateau). This, however, is in partial contradiction to our finding of a very good match between the UV P Cygni profiles of the OHG GS Mus, but aligned with the mismatch for HD151804, which has a much higher v_∞ .

4.2. The $v_\infty - T_{\text{eff}}$ relation

From $v_\infty \propto v_{\text{esc},\Gamma}$ and the Stephan-Boltzmann equation, one can derive the relation

$$v_\infty = C(\kappa[X_{\text{He}}, Z, \rho, f_{\text{cl}}]) L^{1/4} T_{\text{eff}} \sqrt{\frac{1 - \Gamma_e}{\Gamma_e}}, \quad (5)$$

where C is a constant that depends on the opacity κ , which depends on the chemical composition (X_{He} , Z), density ρ and clumping factor f_{cl} . This relation explains the empirical scaling of v_∞ with T_{eff} . In Fig. 10, we plot our resulting values using $T_{\text{eff}} = T_{2/3}$. The different dense and airy solutions leave clear imprints as they show different slopes in the $v_\infty - T_{\text{eff}}$ relation with sharp breaks precisely where the wind gets denser (i.e., in the dense-wind plateaus). While there is more scatter for the hotter models, the airy solutions generally match the empirically obtained slope from Hawcroft et al. (2024) (though shifted in T_{eff} for the cooler valley), while in the dense-wind regimes the relation becomes much flatter.

In Fig. 10, we also plot recent other temperature sequences of hydrodynamically consistent models (with otherwise homogeneous parameters) across the OB and WR regime. Other studies with $\Gamma_e \sim 0.3$, tend to align well with the slope of Hawcroft et al.’s relation. Likewise, when their winds get thicker, the slopes become flatter. While the slopes in the dense-wind regime do not align with those of the WR models from Sander et al. (2023), where we show the $12.9 M_\odot$ sequence with $\Gamma_e \approx 0.32$, the thin-wind regime also matches the (shifted) empirical relation by Hawcroft et al. (2024), indicating that it might be generally valid throughout the whole line-driven wind regime down to ~ 10 kK, independent of Γ_e , as long as the winds do not get dense. Indeed, even the near-Eddington models from Lefever et al. (2025) align mostly with the Hawcroft et al. (2024) slope, similar to our airy wind solutions with a departure towards the trend from the WR sequence for $T_{2/3} > 28$ kK.

Below ~ 10 kK, i.e., past the 2-BiSJ, the stars approach the edge of the line-driven wind regime and their mass loss might be generated and sustained by other sources, like thermal and/or turbulent pressure and pulsations (e.g., Glatzel & Kraus 2024; Glatzel & Kiriakidis 1993; Fadeyev 2010). As discussed above, our models in this temperature regime have most of the outer wind sustained by gas and turbulent pressure. Turbulent pressure also plays a role in launching, although radiative acceleration remains the major contributor there as shown in Fig. B.1 and Fig. B.2. For the coolest models, the dependence on the turbulence is strongest as a viable wind (i.e., $\Gamma_{\text{wind}} > 1$) should not happen without this term and different values of v_{turb} will change v_∞ . This can also be seen in Fig. 10, where the model sequence of Sabhahit et al. (2025) with similar $T_{2/3}$ have v_∞ show higher values precisely due to a much higher $v_{\text{turb}} = 70 \text{ km s}^{-1}$.

4.3. Interpretation of the mass-loss trend and comparison with existing recipes

As shown in Sect. 3, our obtained \dot{M} trend with “plateaus” and “valleys” is benchmarked by the resemblance of the cor-

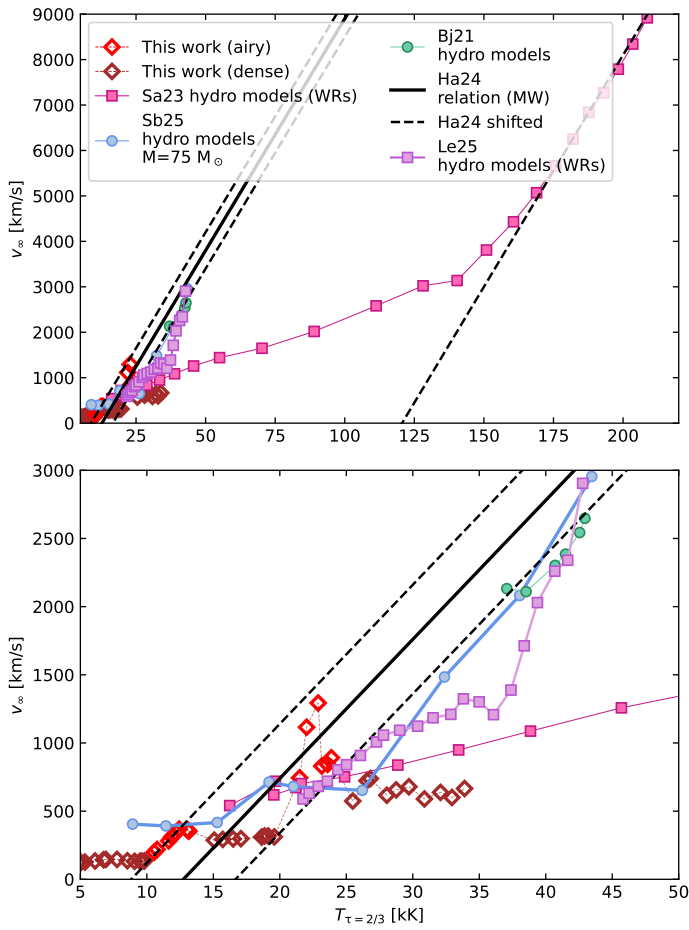


Fig. 10. Relation of v_{∞} – T_{eff} for different studies which made hydrodynamically consistent sequences of models varying T_{\star} . The black lines indicate the empirical relation by Hawcroft et al. (2024) (solid represents the actual relation and the dashed indicate the relation arbitrarily shifted). The pink and violet squares indicate the models by Sander et al. (2023) and Lefever et al. (2025) respectively. Blue circle indicate the models of Sabhahit et al. (2025) with $\Gamma_e \sim 0.35$ whereas the green indicate the models of Björklund et al. (2021) with similar Γ_e . The red and brown diamonds indicate our sequence of models discriminating between the airy and dense solutions respectively.

responding synthetic spectra to several hypergiants/LBs across the OBA star domain and thus should capture the atmospheric physics in this high- Γ_e regime. The jumps in \dot{M} (1-BiSJ and 2-BiSJ) are clearly caused by the recombination of Fe as predicted by Vink et al. (1999). In contrast, there are no clear jumps observed in BSGs despite changes in Fe ionization at the base of the wind (e.g., Bernini-Peron et al. 2023, 2024; de Burgos et al. 2024; Alkousa et al. 2025). This clearly points to a difference originating to first order due to the proximity to the Eddington limit as the BSGs are in a lower Γ_e regime. Together with the recent calculations in Sabhahit et al. (2025) probing different Γ_e -sequences (although with fixed L), the complexity of the derived trend and the bi-stability of the solutions obtained near the jumps suggest a general bi-modality of dense and airy wind solutions. For sufficient conditions, a dense wind solution with high mass-loss rates can be reached where \dot{M} even seems to increase with decreasing temperature. However, if these conditions are not met, the solutions switch to the airy branch, where mass-loss rates tend to decline with decreasing temperature. Adopting this generalized paradigm, the spectra of our findings reveal that hypergiants and some late-type LBs reside in a transition do-

main where the atmospheric conditions can switch between airy and dense solutions depending on the temperature.

While the two solutions do not correspond to the transition to optically-thick winds (i.e., $\tau_{\text{crit}} > 1$), the transition is still triggered by the availability or absence of sufficient opacity (plus turbulent pressure), thus marking a striking similarity with the regime differences found for stripped, He-burning stars in Sander & Vink (2020) and Sander et al. (2023). Comparing our findings with the different sequences from Sabhahit et al. (2025) and Björklund et al. (2023), we suggest that depending on Γ_e there might be no switch between dense and airy regimes as for high Γ_e (and sufficient metallicity, see below) the whole sequence can be in the dense-wind regime where continuum and geometrical effects will dominate. In contrast, for low Γ_e all solutions fall onto the airy branch, as likely happening in the models from Björklund et al. (2023) and Krtička et al. (2024, 2025). However, to confirm this hypothesis, a systematic exploration of the precise conditions is required to isolate the contributions of “supplementary effects” such as clumping and turbulent pressure.

Comparing with existing mass-loss recipes, we find that the recipe from Krtička et al. (2024) applied to our model properties (considering $T_{2/3}$) matches very well the \dot{M} of our models in the airy-wind regime. Their recipe successfully reproduces the typical mass-loss rates determined for cooler BSGs (e.g., Bernini-Peron et al. 2023, 2024; Verhamme et al. 2024). Krtička et al. recipe also predicts a mild increase at the warm plateau region, albeit with a temperature offset. The Björklund et al. (2023) recipe (applied to $T_{2/3}$) matches very well in the hot plateau and relatively cool valley, but underestimates \dot{M} for cooler temperatures. When compared to Vink et al. (2001, applied to $T_{2/3}$), we find a decent match to our sequence up to the cool valley with a systematic offset of 0.8 dex. Interestingly, if we apply Vink et al. to our sequence, considering T_{\star} and shifting the results down by this offset, we obtain an excellent match with our results for the hot plateau, hot valley, and warm plateau (including the 1-BiSJ). All the recipes fail catastrophically to explain the behavior past the 2-BiSJ. At the coolest temperatures, the unscaled Vink et al. rates match again with our derived \dot{M} values.

4.4. The impact of metallicity on the cool models

One of the most striking results of our study is the increase in \dot{M} towards the coolest temperatures. As we discussed above, this is considerably different from what has been obtained in recent modeling efforts in the B supergiant regime. To investigate in particular the increase due to the ionization change from Fe III to Fe II, we also create auxiliary smaller sequences for a fixed $T_{\star} = 16.1$ kK in this regime where we change the He composition and metallicity. In Fig. 12, we present the results where we vary the metallicity of the model and hence also the Fe content. It is noticeable that between 0.7 and 0.6 Z_{\odot} , \dot{M} drops by 1.5 dex, causing the models to switch back to an airy solution.

This additional sequence confirms the importance of line opacities to switch between the two regimes, boosted in particular by the recombination of Fe III to Fe II. The Fe II opacities cause the mass-loss rates to increase, thus increasing the wind density. This, in turn, causes H to recombine and further reduce the wind temperature. When Z is sufficiently low, the wind is thinner, which allows more photons to ionize Fe II into Fe III. As noticeable in Fig. 12, the relative role of the pressure term tends to increase while the shift in the Fe ion dominance happens, which we also find in the main model sequence (cf. Fig. 5). A similar Z -dependence of a solution regime change seems to happen for the Fe IV to Fe III transition in the models in Lefever et al. (2025),

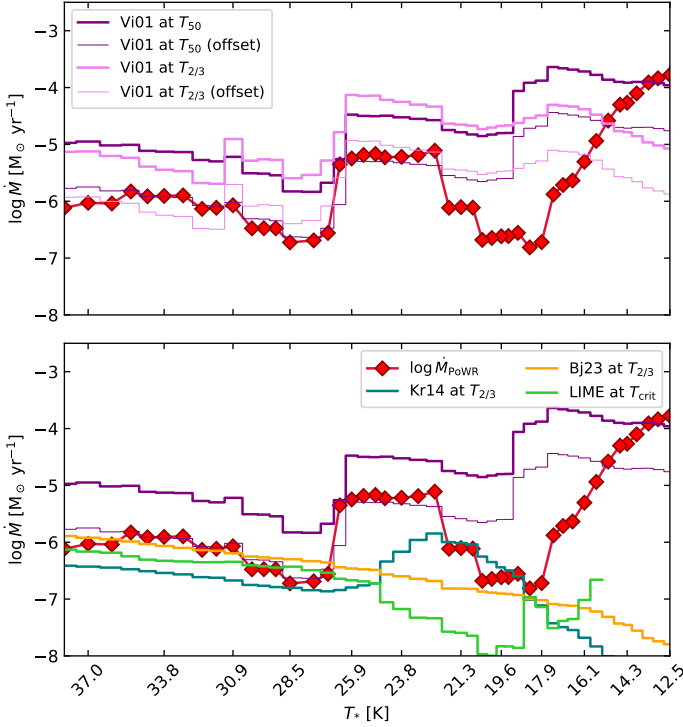


Fig. 11. Comparison between the output mass-loss rates of the T_* sequence (red curve) and different recipes applied to the stellar properties of each model. The thick purple and fuchsia lines indicate the mass-loss rates by Vink et al. (2001) applied, respectively to the T_* and $T_{2/3}$. The thin lines of the same colors indicate the Vink's rates with an offset of 0.8 dex. The yellow curve indicate the rates of Björklund et al. (2023) and the teal line indicate the rates of Krtička et al. (2024) – both applied to $T_{2/3}$. The green line indicate the rates computed using the LIME tool (<https://lime.ster.kuleuven.be/>, Sundqvist et al. 2025)

where a sharp transition in the \dot{M} trend occurs between $0.8 Z_\odot$ and $0.2 Z_\odot$ while a more smooth behavior is found at the highest and lowest Z . This would indicate that for the lowest metallicity,

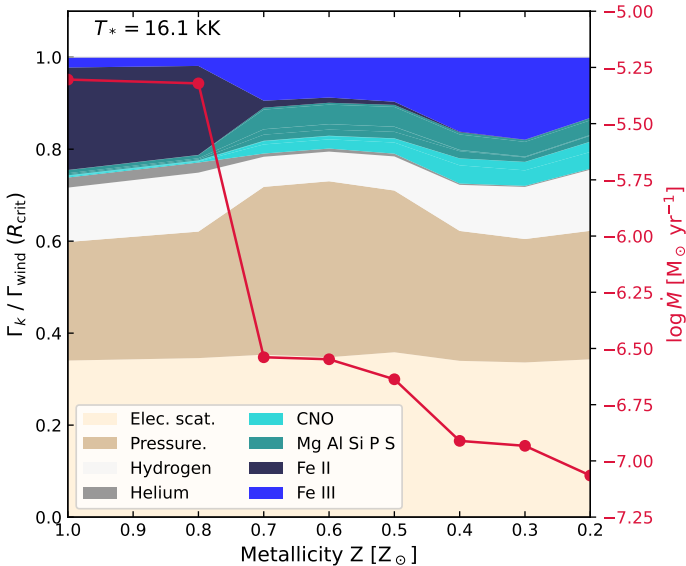


Fig. 12. Contribution to the radiative acceleration from different sources/elements/ions (stacked colored areas) and mass-loss rates (red curve) according to metallicity for a fixed temperature of $T_* = 16.1$ kK.

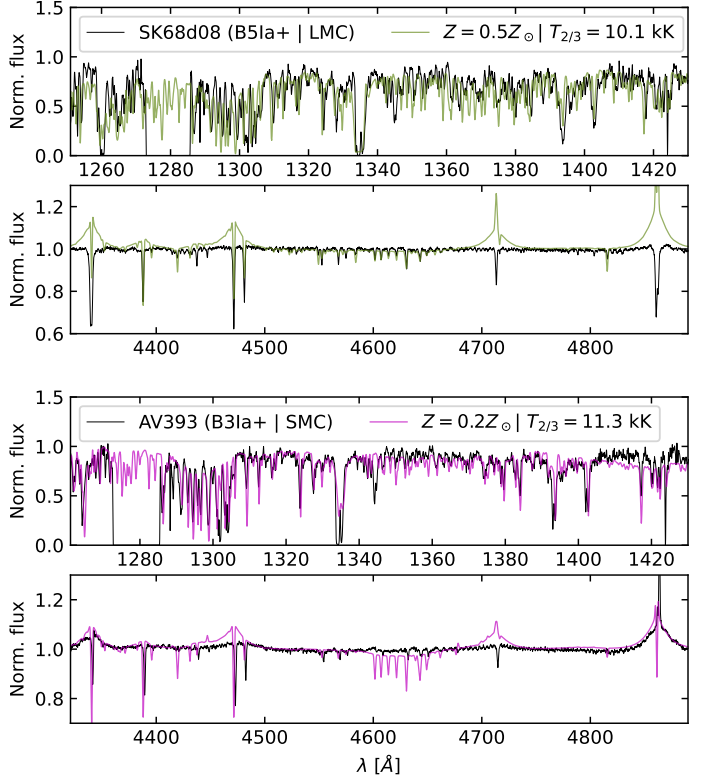


Fig. 13. Non-tailored comparison between the $0.5 Z_\odot$ and $0.2 Z_\odot$ models (olive and violet lines respectively) with the observed spectra of the BHGs SK -68°08 (B5Ia+, in the LMC) and AzV 393 (B3Ia+, in the SMC) – represented by black lines.

all solutions are in the airy branch, while at the highest Z the solutions might all be in the dense branch.

Similar to the solar-metallicity sequence, we also find existing late-type BHGs in the LMC and SMC resembling the normalized spectra resulting from our lower- Z models. Namely, for $Z = 0.2 Z_\odot$, we find a good match between the late BHGs AzV 393 (B3Ia+, SMC) and the synthetic UV and optical spectra – see Fig. 13. For $Z = 0.5 Z_\odot$ we also find signatures comparable to the late BHG Sk -68°08 (B5Ia+, LMC). These stars in particular have L , M , and X_{He} values very similar to our metallicity model sequence (Verhamme et al. 2024, Alkousa et al. 2026), such that the spectral mismatches, especially a systematic excess in the electron scattering wings, could be an indication of a different clumping stratification, which in case of hydrodynamically consistent models, influences the output atmosphere structure and spectrum.

4.5. Comparisons with Yellow Hypergiants

When comparing the position in the HRD and sHRD of our models against the positions of some known Yellow Hypergiants (YHGs), we notice an overlap between their empirically obtained T_{eff} (e.g., Nieuwenhuijzen & de Jager 2000; Nieuwenhuijzen et al. 2012; Kasikov et al. 2024) and our coolest models. Taking V509 Cas as a representative example, the effective temperature after the year 2000 remains consistently between ~ 7.5 and ~ 8.2 kK (Kasikov et al. 2024). Considering the T_{eff} and $\log g$ values from Nieuwenhuijzen et al. (2012), we find that our model sequence crosses essentially orthogonally the variability track of this star in the sHRD parameter space – see Fig. 14.

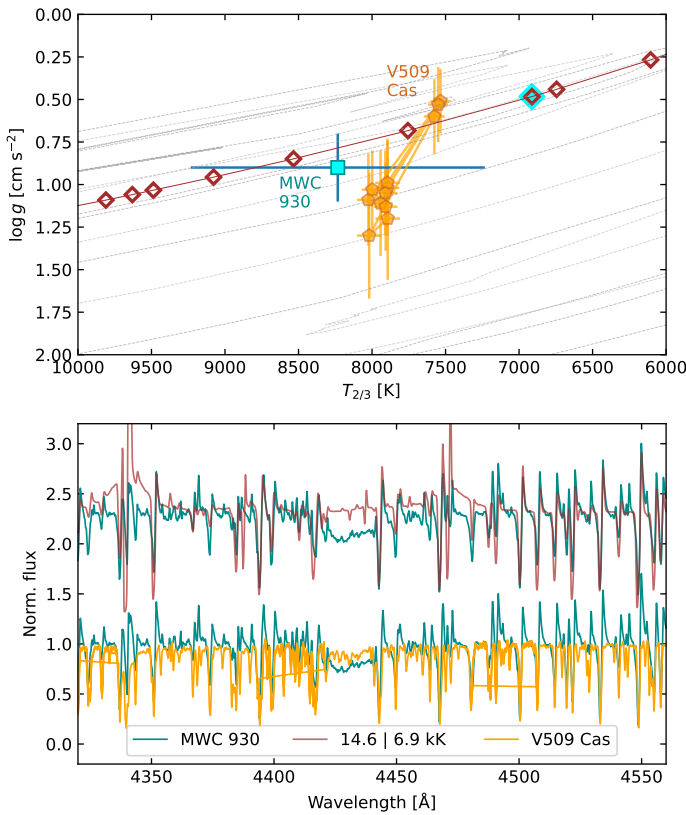


Fig. 14. *Upper panel:* Comparison between our model sequence (brown diamonds), MWC 930 in its maximum (Miroshnichenko et al. 2014, cyan square), and the YHG V509 Cas after 2000 (Nieuwenhuijzen et al. 2012, golden pentagons) in the Kiel Diagram. The cyan diamond marks out the model which most resembles MWC 930. *Lower panel:* Comparison between the respective spectra. The brown curve is our model most similar to MWC 930, the golden curve is the spectrum of V509 Cas in 2012. The spectrum of the LBV is plotted underneath both as a dark cyan line for comparison. The thin dotted line in the background indicates the tracks of Ekström et al. (2012).

In the lower panel of Fig. 14, we compare the spectrum of the YHG V509 Cas to that of the LBV MWC 930 during its maximum, which is closely resembled by our model with $T_\star = 14.6 \text{ kK}$. It is evident that the LBV-type spectrum essentially resembles the YHG spectrum, but is enhanced by wind features. Notably, both stars actually have $T_{2/3} \ll 10 \text{ kK}$, but in the LBV case this is due to the photosphere being formed beyond the critical point, thus not representing the T_{eff} of the (quasi-)hydrostatic atmosphere. In fact, our model resembling MWC 930 has $T_{2/3} \sim 7 \text{ kK}$ while V509 Cas is formally hotter.

The formal distinction between supergiants and hypergiants in the yellow regime is different from that in the BA-star regime and is not based on the same spectroscopic criterion used for OBA hypergiants (e.g., de Jager 1998; Kasikov et al. 2026). Therefore, LBVs such as MWC 930 in its maximum might very well be what more extreme BHGs with dense winds are to BSGs or even BHGs in the airy regime. While our model sequence does not extend to cooler temperatures where Fe I becomes more important, the trend of finding airy solutions when the Fe ionization stage at $r \sim R_{\text{crit}}$ is shifting suggests that another airy wind regime could appear at even cooler T_\star , which could then produce observed YHG spectra like V509 Cas.

5. Conclusions

In this work, we conducted a thorough analysis with hydrodynamically-consistent atmosphere models of a parameter space representative of OBA hypergiants and LBVs at solar metallicity to investigate their mass-loss rates and wind velocity structure across this crucial snapshot in the evolution of high-mass stars. We highlight the following conclusions:

- We find two solution branches, which we describe as “dense” and “airy”. In the explored temperature sequence, the models mainly settle on the dense solution, but cannot maintain this in certain parameter regions. These regions appear as “valleys” in the $\dot{M}(T_{\text{eff}})$ diagram. The “dense” solutions are associated with higher wind optical depths, but do not require values exceeding unity. Instead, the “airy” solutions in this work can be described by $R_t > 200 R_\odot$, though more work is needed to check if this value is universal.
- The normalized spectra synthesized from our models resemble the main spectral appearance of various OBA hypergiants and LBVs. Spectral resemblance is found both for “dense” and for “airy” solutions. Exemplary calculations indicate that these findings could even hold at lower metallicity.
- We find that the contributions of the electron scattering and thermal pressure components are responsible for $\sim 50\%$ of the force at the wind onset (i.e., critical point).
- Our model sequence results are in line with recent near-Eddington PoWR^{HD} calculations employing different luminosities and masses than in our study. Sabhahit et al. (2025) also find valley-like features in some of their $\dot{M}(T_\star)$ sequences, in particular those matching our Γ_e -regime and further away from the Eddington Limit. The higher- Γ_e models calculated by Lefever et al. (2025) at solar metallicity do not display the pronounced valleys, but seem to be in a transition regime between our solutions and even higher Γ_e -sequences in Sabhahit et al. (2025). However, the \dot{M} jumps occurring at lower metallicities in Lefever et al. (2025) show clear similarities to the jumps obtained in this work.
- In contrast to modelling efforts for OB stars, we find a general increase in the mass-loss rate with decreasing temperature. We suggest that this behavior might be exclusive to the “dense” branch. The solutions in the “airy” branch are notably supported by turbulent pressure and our absolute results thus differ from calculations such as Björklund et al. (2023) and Krtička et al. (2024), although there is a partial matching with each of the recipes in some temperature regimes. Down to $T_\star \approx 22 \text{ kK}$, our derived mass-loss pattern matches well with the Vink et al. (2001) prediction if shifted downwards by 0.8 dex.
- The solution switches from “airy” to “dense” in our sequence when Fe recombines such that Fe III or Fe II respectively can provide significant opacity at the critical point. This sharp increase in the mass-loss rate coincides with the traditional “bi-stability jumps” from Vink et al. (1999). We also find an actual bistability of solutions at these jumps.
- For LBVs/P Cygni supergiants with dense winds on the cool side of the second jump, the terminal velocity is well traced by the H lines, but not necessarily by the He I lines.
- We find that the empirical linear relation by Hawcroft et al. (2024) of the wind terminal velocity with the stars’ photospheric temperature seems to be valid for all airy-winded stars “safely” in the line-driven wind regime ($T_{\text{eff}} \gtrsim 10 \text{ kK}$), i.e., valid from late BHGs to WRs. However, the different classes of stars seem to have a different offset.

- We provide updated luminosities for galactic OBA hypergiants and LBVs based on corrected Gaia DR3 parallaxes – when available or applicable. The updated distribution of luminosities causes the population of LBVs/hypergiants – assuming properties publicly available in the literature – to better align with the LBV instability strip. However, careful and thorough analysis is necessary to confirm whether this agreement between theory and empirical findings actually holds.

Acknowledgements. The authors would like to thank A. Kasikov for inspiring discussions and sharing some forthcoming results before publication. The authors would like to thank S. Simón-Díaz and A. de Burgos for providing spectroscopic data from the IACOB project as well as inspiring discussions. MBP and AACs are supported by the Deutsche Forschungsgemeinschaft (DFG, German Research Foundation) in the form of an Emmy Noether Research Group – Project-ID 445674056 (SA4064/1-1, PI Sander). VR acknowledges financial support by the Federal Ministry for Economic Affairs and Energy (BMWE) via the Deutsches Zentrum für Luft- und Raumfahrt (DLR) grant 50 OR 2509 (PI Sander). MBP is a member of the International Max Planck Research School for Astronomy and Cosmic Physics at the University of Heidelberg (IMPRS-HD). This project was co-funded by the European Union (Project 101183150 - OCEANS). Based on observations collected at the European Southern Observatory under ESO programme(s). This work presents results from the European Space Agency (ESA) space mission Gaia. Gaia data are being processed by the Gaia Data Processing and Analysis Consortium (DPAC). Funding for the DPAC is provided by national institutions, in particular the institutions participating in the Gaia MultiLateral Agreement (MLA).

References

Agliozzo, C., Noriega-Crespo, A., Umana, G., et al. 2014, MNRAS, 440, 1391
 Agliozzo, C., Phillips, N., Mehner, A., et al. 2021, A&A, 655, A98
 Alkousa, T., Crowther, P. A., Bestenlehner, J. M., et al. 2025, A&A, 699, A314
 Arun, R., Prasoon, S. A., Mathew, B., et al. 2025, MNRAS, 543, 3214
 Bailer-Jones, C. A. L., Rybizki, J., Fouesneau, M., Demleitner, M., & Andrae, R. 2021, AJ, 161, 147
 Bakhytkyzy, A., Miroshnichenko, A. S., Klochkova, V. G., et al. 2025, Galaxies, 13, 17
 Barneske, A., Osokinova, L. M., & Hamann, W.-R. 2008, A&A, 486, 971
 Berlanas, S. R., Herrero, A., Comerón, F., et al. 2020, A&A, 642, A168
 Bernini-Peron, M., Marcolino, W. L. F., Sander, A. A. C., et al. 2023, A&A, 677, A50
 Bernini-Peron, M., Sander, A. A. C., Najarro, F., et al. 2025, A&A, 697, A41
 Bernini-Peron, M., Sander, A. A. C., Ramachandran, V., et al. 2024, A&A, 692, A89
 Björklund, R., Sundqvist, J. O., Puls, J., & Najarro, F. 2021, A&A, 648, A36
 Björklund, R., Sundqvist, J. O., Singh, S. M., Puls, J., & Najarro, F. 2023, A&A, 676, A109
 Cardelli, J. A., Clayton, G. C., & Mathis, J. S. 1989, ApJ, 345, 245
 Carretero-Castrillo, M., Ribó, M., & Paredes, J. M. 2023, A&A, 679, A109
 Castor, J. I., Abbott, D. C., & Klein, R. I. 1975, ApJ, 195, 157
 Chentov, E. L. & Luud, L. 1989, Astrophysics, 31, 415
 Clark, J. S., Crowther, P. A., Larionov, V. M., et al. 2009a, A&A, 507, 1555
 Clark, J. S., Davies, B., Najarro, F., et al. 2009b, A&A, 504, 429
 Clark, J. S., Egan, M. P., Crowther, P. A., et al. 2003, A&A, 412, 185
 Clark, J. S., Najarro, F., Negueruela, I., et al. 2012, A&A, 541, A145
 Clark, J. S. & Negueruela, I. 2004, A&A, 413, L15
 Conti, P. S. 1984, in IAU Symposium, Vol. 105, Observational Tests of the Stellar Evolution Theory, ed. A. Maeder & A. Renzini, 233
 Crowther, P. A., Lennon, D. J., & Walborn, N. R. 2006, A&A, 446, 279
 Curé, M., Cidale, L., & Granada, A. 2011, ApJ, 737, 18
 Cutri, R. M., Wright, E. L., Conrow, T., et al. 2013, Explanatory Supplement to the AllWISE Data Release Products, Explanatory Supplement to the All-WISE Data Release Products, by R. M. Cutri et al.
 de Burgos, A., Keszthelyi, Z., Simón-Díaz, S., & Urbaneja, M. A. 2024, A&A, 687, L16
 de Jager, C. 1998, A&A Rev., 8, 145
 de Jager, C., Nieuwenhuijzen, H., & van der Hucht, K. A. 1988, A&AS, 72, 259
 Debnath, D., Sundqvist, J. O., Moens, N., et al. 2024, A&A, 684, A177
 Driessens, F. A., Sundqvist, J. O., & Kee, N. D. 2019, A&A, 631, A172
 Egan, M. P., Clark, J. S., Mizuno, D. R., et al. 2002, ApJ, 572, 288
 Ekström, S., Georgy, C., Eggenberger, P., et al. 2012, A&A, 537, A146
 Fadeyev, Y. A. 2010, Astronomy Letters, 36, 362
 Gaia Collaboration, Vallenari, A., Brown, A. G. A., et al. 2023, A&A, 674, A1
 Glatzel, W. & Kiriakidis, M. 1993, MNRAS, 263, 375
 Glatzel, W. & Kraus, M. 2024, MNRAS, 529, 4947
 Gräfener, G., Koesterke, L., & Hamann, W. R. 2002, A&A, 387, 244
 Groh, J. H., Hillier, D. J., & Damineli, A. 2011, ApJ, 736, 46
 Groh, J. H., Hillier, D. J., Damineli, A., et al. 2009, ApJ, 698, 1698
 Groh, J. H., Hillier, D. J., Madura, T. I., & Weigelt, G. 2012, MNRAS, 423, 1623
 Gvaramadze, V. V. & Menten, K. M. 2012, A&A, 541, A7
 Haucke, M., Cidale, L. S., Venero, R. O. J., et al. 2018, A&A, 614, A91
 Hawcroft, C., Sana, H., Mahy, L., et al. 2024, A&A, 688, A105
 Hillier, D. J., Crowther, P. A., Najarro, F., & Fullerton, A. W. 1998, A&A, 340, 483
 Holgado, G., Simón-Díaz, S., Haemmerlé, L., et al. 2020, A&A, 638, A157
 Humphreys, R. M. & Davidson, K. 1979, ApJ, 232, 409
 Hur, H., Lim, B., & Chun, M.-Y. 2023, Journal of Korean Astronomical Society, 56, 97
 Kasikov, A., Kolka, I., Aret, A., Eenmäe, T., & Checha, V. 2024, A&A, 686, A270
 Kasikov, A., Mehner, A., Kolka, I., & Aret, A. 2026, A&A, submitted
 Kee, N. D., Sundqvist, J. O., Decin, L., de Koter, A., & Sana, H. 2021, A&A, 646, A180
 Klochkova, V. G. 2019, Astrophysical Bulletin, 74, 475
 Kniazev, A. Y., Gvaramadze, V. V., & Berdnikov, L. N. 2016, MNRAS, 459, 3068
 Kotak, R. & Vink, J. S. 2006, A&A, 460, L5
 Krtička, J., Kubát, J., & Krtičková, I. 2024, A&A, 681, A29
 Krtička, J., Kubát, J., & Krtičková, I. 2025, A&A, 702, A9
 Lamers, H. J. G. L. M., Snow, T. P., & Lindholm, D. M. 1995, ApJ, 455, 269
 Langer, N. 2012, ARA&A, 50, 107
 Larkin, C. J. K., Hawcroft, C., Mackey, J., et al. 2025a, A&A, 703, L14
 Larkin, C. J. K., Mackey, J., Haworth, T. J., & Sander, A. A. C. 2025b, A&A, 700, A60
 Lefever, K., Puls, J., & Aerts, C. 2007, A&A, 463, 1093
 Lefever, R. R., Sander, A. A. C., Bernini-Peron, M., et al. 2025, A&A, 700, A2
 Lefever, R. R., Sander, A. A. C., González-Torà, G., et al. 2026, A&A, submitted
 Lefever, R. R., Sander, A. A. C., Shenar, T., et al. 2023, MNRAS, 521, 1374
 Leung, H. W., Bovy, J., Mackereth, J. T., et al. 2023, MNRAS, 519, 948
 Lobel, A., Groh, J. H., Martayan, C., et al. 2013, A&A, 559, A16
 Mahy, L., Hutsemékers, D., Royer, P., & Waelkens, C. 2016, A&A, 594, A94
 Markova, N. & Puls, J. 2008, A&A, 478, 823
 Martins, F., Genzel, R., Hillier, D. J., et al. 2007, A&A, 468, 233
 Maryeva, O. V., Karpov, S. V., Kniazev, A. Y., & Gvaramadze, V. V. 2022, MNRAS, 513, 5752
 Miroshnichenko, A. S., Manset, N., Zharikov, S. V., et al. 2014, Advances in Astronomy, 2014, E7
 Miroshnichenko, A. S., Zharikov, S. V., Vaidman, N. L., & Khokhlov, S. A. 2025, arXiv e-prints, arXiv:2511.13058
 Moens, N., Debnath, D., Verhamme, O., et al. 2025, A&A, 704, A121
 Moens, N., Poniatowski, L. G., Hennicker, L., et al. 2022, A&A, 665, A42
 Müller, P. E. & Vink, J. S. 2008, A&A, 492, 493
 Najarro, F. 1995, PhD thesis, -
 Najarro, F., Figer, D. F., Hillier, D. J., Geballe, T. R., & Kudritzki, R. P. 2009, ApJ, 691, 1816
 Najarro, F., Krabbe, A., Genzel, R., et al. 1997, A&A, 325, 700
 Nazé, Y., Rauw, G., & Hutsemékers, D. 2012, A&A, 538, A47
 Negueruela, I., Alfaro, E. J., Dorda, R., et al. 2022, A&A, 664, A146
 Negueruela, I., Simón-Díaz, S., de Burgos, A., Casasbuenas, A., & Beck, P. G. 2024, A&A, 690, A176
 Nieuwenhuijzen, H. & de Jager, C. 2000, A&A, 353, 163
 Nieuwenhuijzen, H., De Jager, C., Kolka, I., et al. 2012, A&A, 546, A105
 Nyholm, A., Sollerman, J., Tartaglia, L., et al. 2020, A&A, 637, A73
 Pasquali, A., Comerón, F., & Nota, A. 2006, A&A, 448, 589
 Pauldrach, A., Puls, J., & Kudritzki, R. P. 1986, A&A, 164, 86
 Pauldrach, A. W. A. & Puls, J. 1990, A&A, 237, 409
 Paunzen, E. 2022, A&A, 661, A89
 Petriella, A., Paron, S. A., & Giacani, E. B. 2012, A&A, 538, A14
 Petrov, B., Vink, J. S., & Gräfener, G. 2016, MNRAS, 458, 1999
 Prinja, R. K., Barlow, M. J., & Howarth, I. D. 1990, ApJ, 361, 607
 Ritchie, B. W., Clark, J. S., Negueruela, I., & Najarro, F. 2009, A&A, 507, 1597
 Rivet, J.-P., Siciak, A., de Almeida, E. S. G., et al. 2020, MNRAS, 494, 218
 Rubio-Díez, M. M., Sundqvist, J. O., Najarro, F., et al. 2022, A&A, 658, A61
 Sabhahit, G. N., Vink, J. S., & Sander, A. A. C. 2025, arXiv e-prints, arXiv:2512.13782
 Sander, A. A. C., Fürst, F., Kretschmar, P., et al. 2018, A&A, 610, A60
 Sander, A. A. C., Lefever, R. R., Poniatowski, L. G., et al. 2023, A&A, 670, A83
 Sander, A. A. C. & Vink, J. S. 2020, MNRAS, 499, 873
 Sander, A. A. C., Vink, J. S., & Hamann, W.-R. 2020, MNRAS, 491, 4406
 Searle, S. C., Prinja, R. K., Massa, D., & Ryans, R. 2008, A&A, 481, 777
 Smith, N. 2006, ApJ, 644, 1151
 Smith, N. 2014, ARA&A, 52, 487
 Smith, N. 2019, MNRAS, 488, 1760
 Smith, N. & Stassun, K. G. 2017, AJ, 153, 125
 Sterken, C., Gosset, E., Juttner, A., et al. 1991, A&A, 247, 383

Stothers, R. B. 2003, *ApJ*, 589, 960
 Sundqvist, J. O., Debnath, D., Backs, F., et al. 2025, *A&A*, 703, A284
 Trundle, C., Kotak, R., Vink, J. S., & Meikle, W. P. S. 2008, *A&A*, 483, L47
 Ueta, T., Meixner, M., Dayal, A., et al. 2001, *ApJ*, 548, 1020
 van Genderen, A. M. 2001, *A&A*, 366, 508
 Verhamme, O., Sundqvist, J., de Koter, A., et al. 2024, *A&A*, 692, A91
 Vieu, T., Larkin, C. J. K., Häger, L., et al. 2024, *MNRAS*, 532, 2174
 Vink, J. S. 2022, *ARA&A*, 60, 203
 Vink, J. S. & de Koter, A. 2002, *A&A*, 393, 543
 Vink, J. S., de Koter, A., & Lamers, H. J. G. L. M. 1999, *A&A*, 350, 181
 Vink, J. S., de Koter, A., & Lamers, H. J. G. L. M. 2001, *A&A*, 369, 574
 Vink, J. S. & Sander, A. A. C. 2021, *MNRAS*, 504, 2051
 Weßmayer, D., Przybilla, N., & Butler, K. 2022, *A&A*, 668, A92
 Weßmayer, D., Przybilla, N., Ebenbichler, A., Aschenbrenner, P., & Butler, K. 2023, *A&A*, 677, A175
 Zacharias, N., Monet, D. G., Levine, S. E., et al. 2004, in American Astronomical Society Meeting Abstracts, Vol. 205, American Astronomical Society Meeting Abstracts, 48.15

Table A.1. Ions, levels, and transition/lines considered in the models

Elem.	ion	levels	lines	Elem.	ion	levels	lines
H	I	30	435	Mg	I	1	0
H	II	1	0	Mg	II	32	496
He	I	45	990	Mg	III	43	903
He	II	30	435	Mg	IV	17	136
He	III	1	0	Mg	V	20	190
N	I	10	45	Si	I	20	190
N	II	38	703	Si	II	20	190
N	III	85	3570	Si	III	24	276
N	IV	38	703	Si	IV	55	1485
N	V	20	190	Si	V	52	1326
N	VI	14	91	P	IV	12	66
C	I	15	105	P	V	11	55
C	II	32	496	P	VI	1	0
C	III	40	780	Al	I	1	0
C	IV	25	300	Al	II	10	45
C	V	29	406	Al	III	10	45
C	VI	1	0	Al	IV	1	0
O	I	13	78	Fe	I	13	40
O	II	37	666	Fe	II	14	48
O	III	33	528	Fe	III	13	40
O	IV	29	406	Fe	IV	18	77
O	V	54	1431	Fe	V	22	107
O	VI	35	595	Fe	VI	29	194
O	VII	15	105	Fe	VII	19	87
S	II	32	496	Fe	VIII	14	49
S	III	23	253	Fe	IX	15	56
S	IV	25	300	Fe	X	1	0
S	V	20	190				
S	VI	22	231				

Appendix A: Atomic data

In Table A.1, we list the elements and ions with the number of levels and line transitions considered in our atmosphere models. For Fe – which in PoWR refers to all iron-group elements conflated –, the levels and line numbers refer to superlevels and “superlines” (see Gräfener et al. 2002, for more details). The v_{dop} parameter, which controls the resolution of the frequency-dependent cross section of all the elements (Gräfener et al. 2002) is set to the same value of the turbulent motion – i.e., $v_{\text{dop}} = 20 \text{ km s}^{-1}$.

Appendix B: Wind structure in different regimes

In Fig. 5 we compare \dot{M} with the contribution of the main processes, elements, and ions to the wind acceleration at the critical point for each value of T_* . In Fig. B.1 we provide an extension of this figure showing the respective main contributions to the wind driving at different points in the atmosphere. Namely, at $\tau = 20$, near the inner boundary ($\tau = 50$), probing the forces in the inner atmosphere, (ii) at the critical point, where the wind is effectively launched, and (iii) at $\tau = 0.01$, which probes conditions far out in the wind.

A more detailed view on the acceleration structure for representative models at each regime described in Sect. 3 is given in Fig. B.2. In Fig. B.3 we illustrate the velocity structure of models in different regimes. One can see that the turbulent velocity is equal or larger than the sound speed in the wind, indicating that the turbulent pressure dominates over the gas thermal pressure. This is particularly important for models in the cold wall.

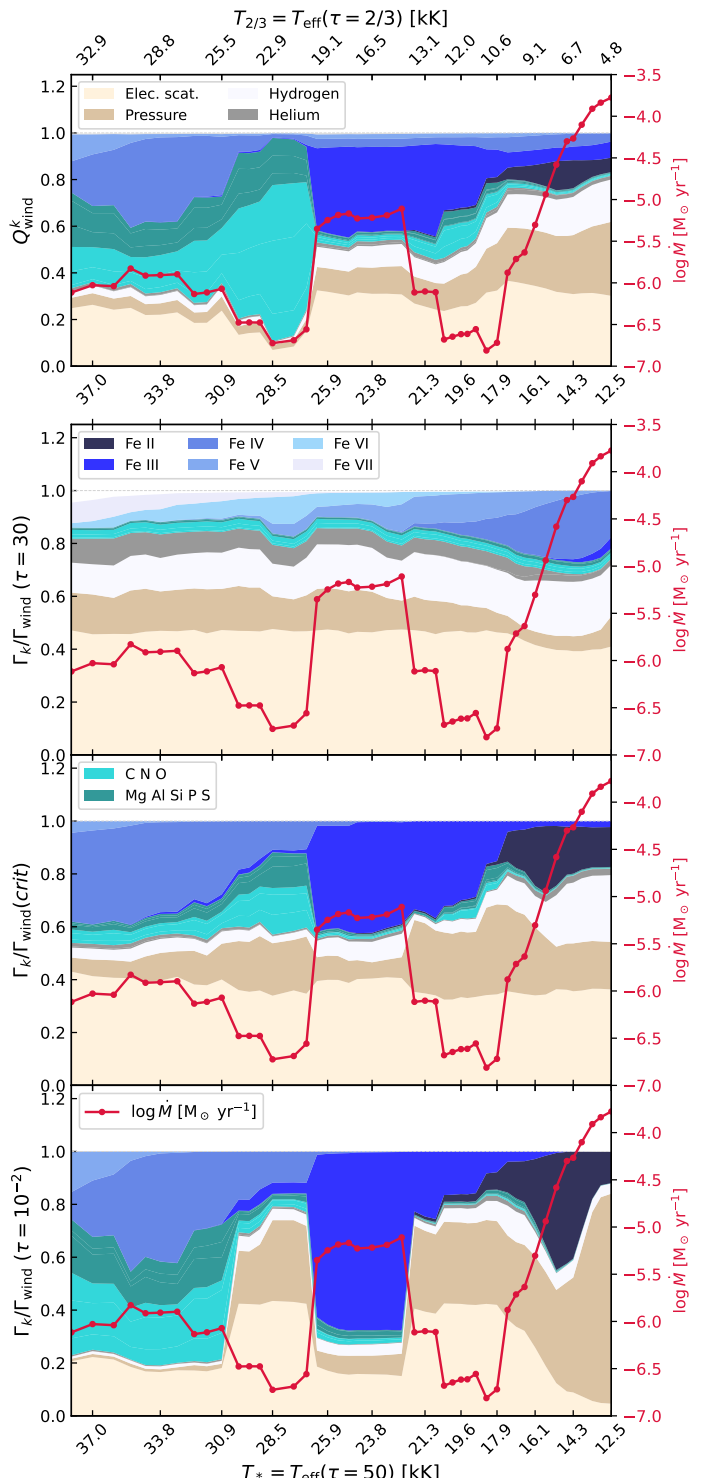


Fig. B.1. *Upper panel:* Contribution of different processes/elements/ions to the wind work ratio Q_{wind} . The other panels indicate each contribution to the wind driving at specific depths – namely, at $\tau = 30$ (near the inner boundary), $\tau = \tau_{\text{crit}}$ (where the wind is launched, like in Fig. 5), and $\tau = 0.01$ (far out in the wind). The color code is the same of Fig. 5.

Appendix C: Bi-stability of solutions at the jumps

When computing hydrodynamically consistent models, the complex interplay between radiation field, species populations, and velocity field does not necessarily converge to unique solutions. Such complexity is due to the non-linearity of the equations be-

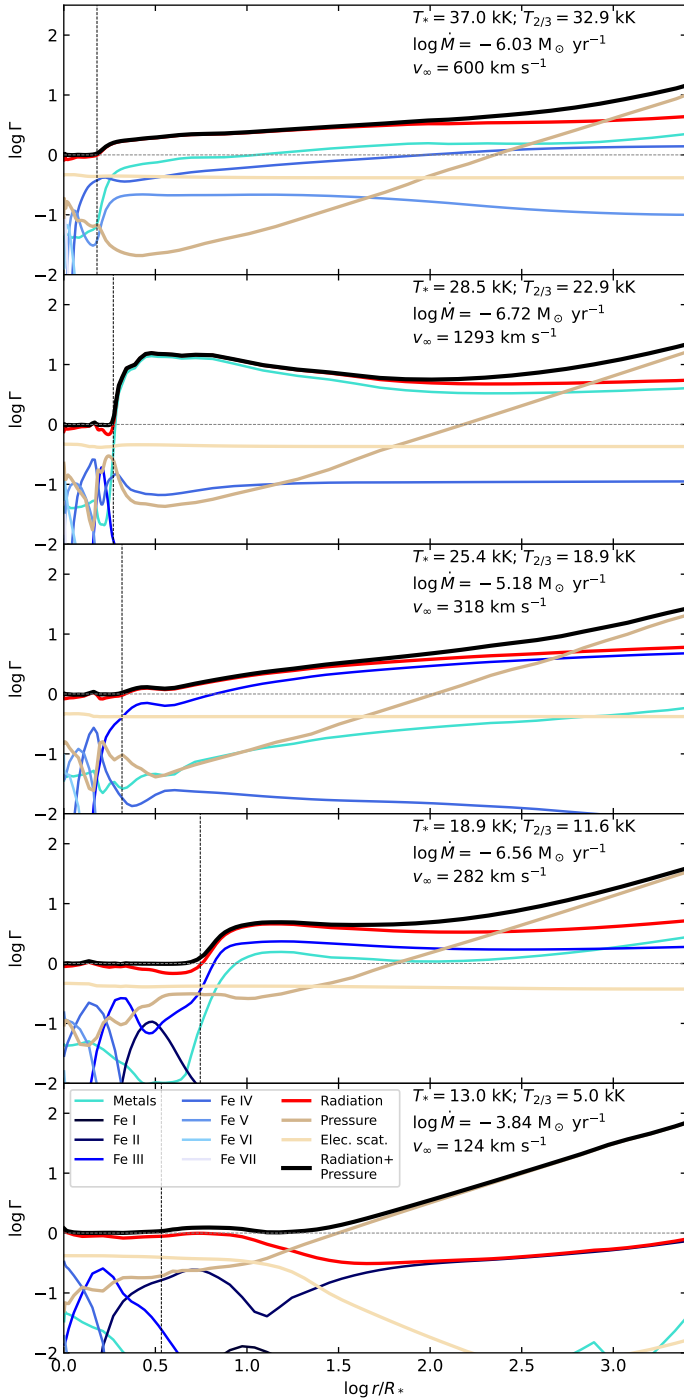


Fig. B.2. Acceleration structure and main contributions to the driving to the atmospheres/winds for models in different wind-solutions domain.

ing solved – coupled both in space and frequency. Therefore, the radiative acceleration structure, obtained via the integration of the momentum equation inwards and outwards from the critical point, depends on conditions elsewhere in the atmosphere/wind.

This means that, for instance, different initial physical conditions can yield different results (with them all satisfying the criteria for numerical convergence) or even fail to reach convergence in case the initial “guess” is far from a valid solution. Given the high computational cost of each model, exhaustively mapping these degeneracies is beyond the scope of this work. However, as a sanity check of the obtained trend, we compute

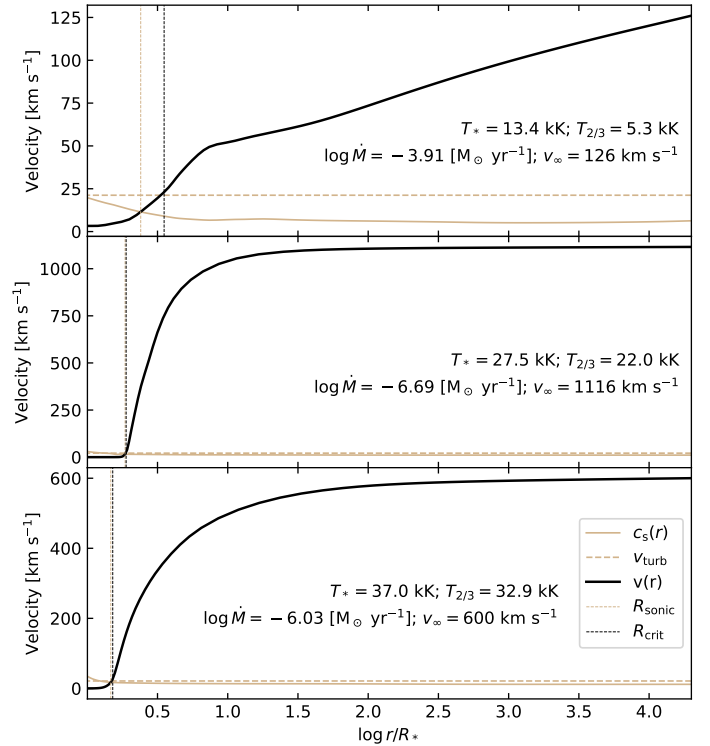


Fig. B.3. Wind velocity structure (black line) for models in the cold wall, hot valley, and hot plateau wind-solution regions. The beige line indicates the sonic speed structure (c_s) while the dotted beige line indicate the turbulent velocity $v_{\text{turb}} = 20 \text{ km s}^{-1}$. The thin vertical lines indicate the sonic radius (R_{sonic} , beige) and critical radius (R_{crit} , black).

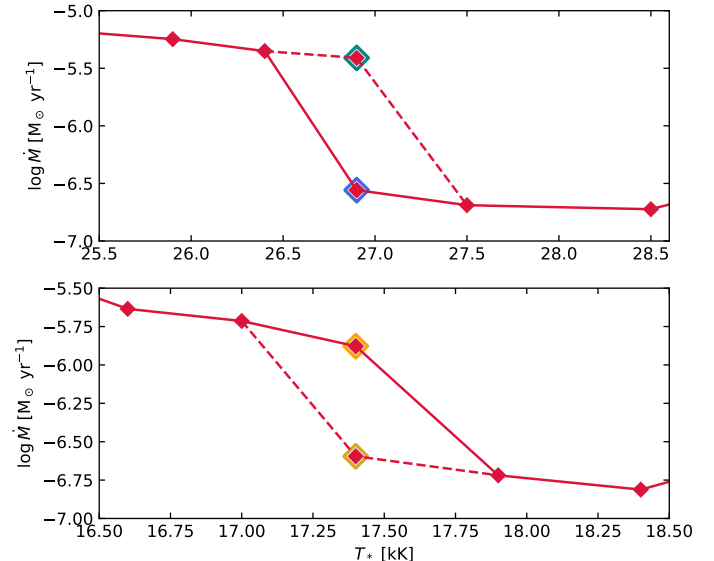


Fig. C.1. Demonstration of the bi-stability of solutions in the 1-BiSJ (upper panel) and 2-BiSJ (lower panel). In either case, we find models with the same T_* yielding different results based on their initial conditions.

models with different initial conditions in distinct regions of our T_{eff} sequence.

This is particularly important when operating in the transition between the “airy” and “dense” solutions. In Fig. C.1, we show that at the edge of the 1-BiSJ and 2-BiSJ, the same T_* can produce different values of \dot{M} when the initial conditions are a model on the airy or on the dense branch.

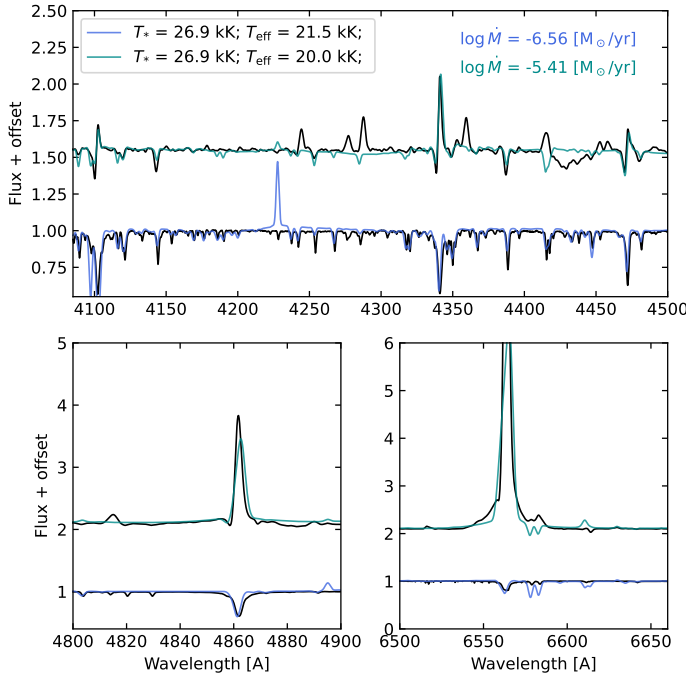


Fig. C.2. Manifestation of the bi-stability of solutions in the model spectrum for the 1-BiSJ in our sequence.

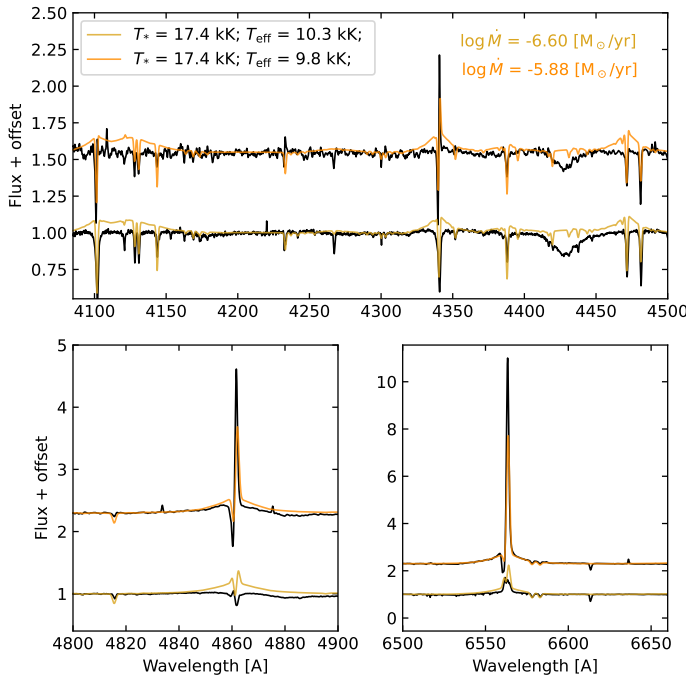


Fig. C.3. Analogous to Fig. C.2 but for the 2-BiSJ.

This also manifests in the spectral appearance of the models' synthetic spectra, which also match different observed stars.

This prohibits us from pinpointing exact simple relations between temperatures (or other parameters) and wind properties. With this exercise, we can also provide a certain interval of confidence in our $\dot{M}(T_{\text{eff}})$ behavior and the associated transition between regimes. However, it indicates that stars with similar properties may exist in different regimes – which recycles the original discussions on bi-stability by Pauldrach & Puls (1990).

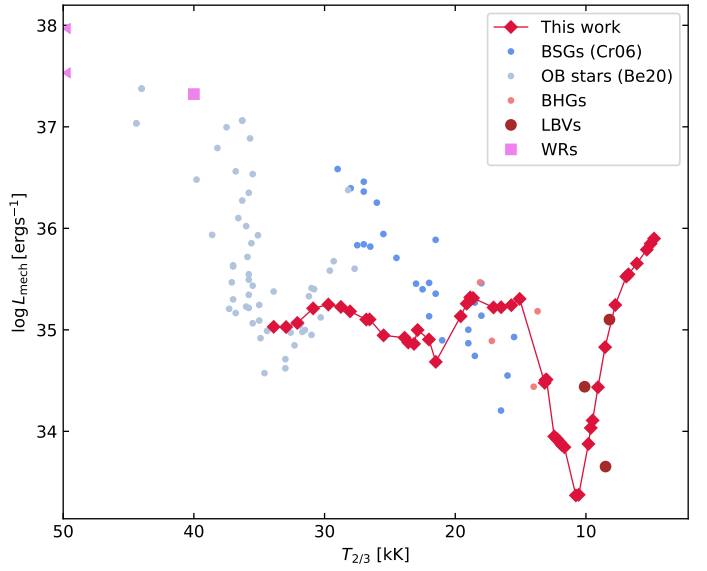


Fig. C.4. Mechanical luminosity of the model sequence compared to literature data from Crowther et al. (2006), Berlanas et al. (2020) – light blue circles –, and WR L_{mech} estimates in Vieu et al. (2024) – pink squares and arrows, which indicate WRs outside the plotting area.

Appendix C.1: Mechanical wind luminosity

To investigate the impact of hypergiants on their environment, we calculate the mechanical wind luminosity $L_{\text{mech}} := 0.5 \dot{M} v_{\infty}^2$. In general, up to the cool airy valley, we find $L_{\text{mech}} \sim 10^{36} \text{ erg s}^{-1}$, comparable to late-O and B stars (see, e.g., Vieu et al. 2024). In the valley, L_{mech} plunges due to the combination of very low \dot{M} and v_{∞} . Past the 2-BiSJ, the high mass-loss rates reached in the cold wall region invert the trend and cause L_{mech} to increase up to $\sim 10^{36} \text{ erg s}^{-1}$. However, the low terminal velocities lead to generally lower L_{mech} values, making hotter stars and in particular Wolf-Rayet stars significantly more important with respect to kinetic feedback unless much higher luminosities and thus mass-loss rates would be reached than mapped in our model sequence. Nonetheless, significant mass loss from cooler massive stars can affect cluster properties via mass loading (e.g., Larkin et al. 2025a,b).

Appendix D: Luminosity of GS Mus (O9.7Ia+) and HD151804 (O8Iaf)

In the literature, we were able to find spectroscopic properties of GS Mus and HD151804 obtained via analysis of the normalized spectra (e.g., Prinja et al. 1990; Holgado et al. 2020). However, we could not find luminosities based on SED fitting. For GS Mus Lefever et al. (2007) derived $\log L/L_{\odot} = 5.75$ based on the V magnitude, spectral type and luminosity class. As our models yielded similar $T_{2/3}$ and $\log g$, we estimated their luminosities via fitting the optical and IR photometric fluxes and flux-calibrated far-UV – see Fig. D.1 and Fig. D.2. The reddening was estimated via fitting the near-UV 2175 Å absorption bump applying the extinction law by Cardelli et al. (1989). As we do not perform a dedicated fitting, we consider a conservative uncertainty of 0.2 dex to the luminosity of each star.

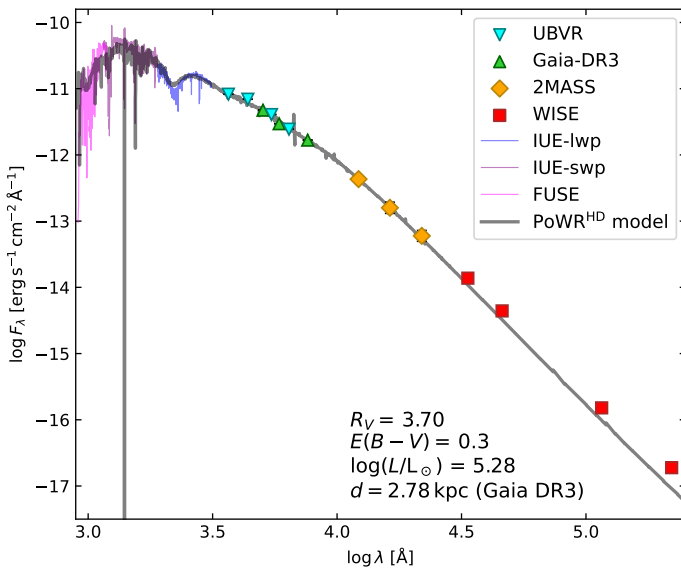


Fig. D.1. Spectral energy distribution of GS Mus. The photometry used in were sourced from Gaia Collaboration et al. (2023), Paunzen (2022), Zacharias et al. (2004), and Cutri et al. (2013).

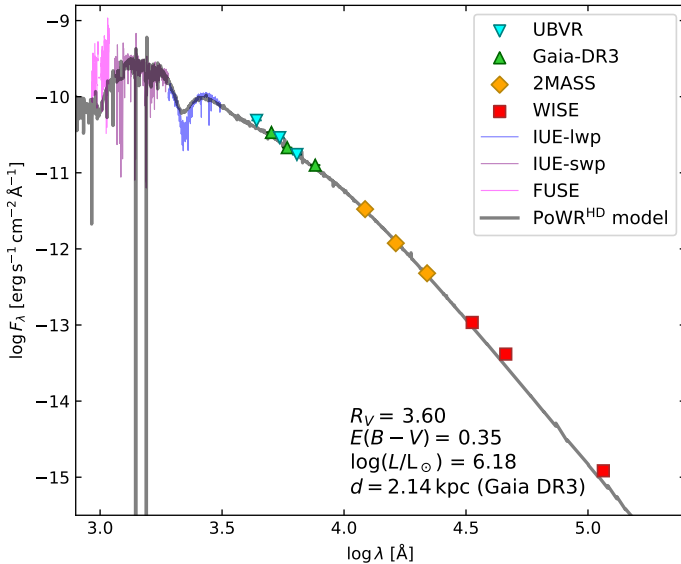


Fig. D.2. Spectral energy distribution of HD151804. The photometry is sourced from the same references as in Fig. D.1.

Appendix E: Model fundamental wind parameters

In Tables E.1 and E.2 we disclose the fundamental atmospheric/wind properties of the sequences of models discussed in this paper.

Appendix F: Luminosities of LBVs and cLBVs with updated distances

To construct the HR diagram in Fig. 1, we first collected literature values of effective temperatures and luminosities of OBA and yellow hypergiants, LBVs, B[e]SG, and yellow supergiants (YSGs). The list of OBA hypergiants and LBVs is largely based on previous literature compilations from Nazé et al. (2012) and Smith et al. (2019). The B[e]SG stars are sourced from Miroshnichenko et al. (2025) and the YHGs and YSGs values are taken from Kasikov et al. (2026). We updated the luminosities based

on updated distance measurements – mostly from the catalog of Bailer-Jones et al. (2021) based on Gaia DR3 parallaxes. We considered the geometric distances listed in their catalog. In Table F.1 we disclose the literature stellar temperatures, luminosities (with the respective distances), and updated luminosities adopting the corresponding new distances.

In general, we do not find a systematic increase in the obtained luminosities compared to previous measurements, a result that differs from what Smith et al. (2019) found when updating previous literature values to Gaia DR2-based distances. Namely, they found an overall reduction in luminosity. However, we find that the population of LBVs with updated distances tends to align much more with the LBV instability strip (Groh et al. 2009). Moreover it seems to connect smoothly with the brightest hot YSGs (the edge of the so-called Yellow Void de Jager 1998), whose luminosities were recently updated by Kasikov et al. (2026).

Table E.1. Atmosphere/wind fundamental properties for each model in the T_\star sequence.

T_\star [kK]	R_\star [R_\odot]	\dot{M} [M_\odot yr $^{-1}$]	$T_{2/3}$ [kK]	R_t [R_\odot]	$\log g$ [cm s $^{-2}$]	$\Gamma_e(R_{\text{crit}})$	$R_{2/3}$ [R_\star]	R_{crit} [R_\star]	R_{sonic} [R_\star]
12.5	131.8	-3.78	4.8	8.69	-0.16	0.39	6.82	3.29	2.18
13	121.9	-3.84	5	8.89	-0.06	0.39	6.63	3.41	2.3
13.4	114.7	-3.91	5.3	9.45	0.04	0.39	6.29	3.52	2.4
13.9	106.6	-4.1	6.1	12.31	0.27	0.39	5.18	3.73	2.58
14.3	100.7	-4.27	6.7	15.67	0.44	0.39	4.5	3.97	2.74
14.6	96.6	-4.3	6.9	16	0.48	0.39	4.46	4.07	2.8
15.1	90.3	-4.58	7.8	23.04	0.68	0.39	3.79	4.95	3.06
15.6	84.6	-4.94	8.5	35.7	0.85	0.38	3.34	6.43	3.67
16.1	79.5	-5.3	9.1	57.31	0.96	0.39	3.15	8.55	4.88
16.6	74.8	-5.64	9.5	89.88	1.03	0.39	3.06	10.59	6.06
17	71.3	-5.71	9.6	97.18	1.06	0.4	3.12	11.24	6.5
17.4	68	-5.88	9.8	119.82	1.09	0.4	3.15	12.5	7.28
17.9	64.3	-6.72	10.6	534.5	1.22	0.42	2.88	11.16	8.33
18.4	60.8	-6.81	10.8	624.17	1.25	0.42	2.92	10.9	8.33
18.9	57.7	-6.56	11.6	472.15	1.39	0.42	2.63	5.56	4.85
19.3	55.3	-6.61	11.9	526.1	1.42	0.42	2.65	5.42	4.79
19.6	53.6	-6.62	12	523.21	1.44	0.42	2.67	5.35	4.76
20	51.5	-6.65	12.2	551.28	1.47	0.42	2.69	5.22	4.7
20.4	49.5	-6.68	12.4	585.08	1.5	0.42	2.7	5.11	4.64
20.8	47.6	-6.11	13	233.92	1.58	0.42	2.55	3.68	3.46
21.3	45.4	-6.1	13.1	217.74	1.59	0.42	2.64	3.78	3.56
21.8	43.3	-6.12	13.2	209.33	1.6	0.42	2.74	3.93	3.71
22.4	41.1	-5.11	15.1	36.98	1.84	0.42	2.21	2.79	2.22
23.1	38.6	-5.19	15.7	39.77	1.91	0.42	2.16	2.8	2.24
23.8	36.4	-5.22	16.5	39.43	1.99	0.42	2.08	2.55	2.18
24.5	34.3	-5.23	17.1	37.88	2.05	0.42	2.06	2.49	2.18
24.9	33.2	-5.17	18.6	34.4	2.21	0.42	1.78	2.05	1.86
25.4	31.9	-5.18	18.9	34.51	2.23	0.42	1.82	2.08	1.91
25.9	30.7	-5.25	19.1	36.52	2.25	0.42	1.83	2.13	1.98
26.4	29.6	-5.35	19.6	40.63	2.29	0.42	1.82	2.15	2
26.9	28.5	-6.56	21.5	446.88	2.45	0.43	1.57	1.91	1.88
27.5	27.2	-6.69	22	684.35	2.5	0.43	1.56	1.89	1.86
28.5	25.4	-6.72	22.9	742.22	2.56	0.43	1.55	1.86	1.83
29.1	24.3	-6.48	23.2	361.98	2.58	0.43	1.58	1.99	1.95
29.6	23.5	-6.48	23.6	352.5	2.62	0.43	1.57	1.99	1.95
30.1	22.7	-6.48	23.9	355.45	2.64	0.43	1.59	1.99	1.95
30.9	21.6	-6.07	25.5	134.72	2.75	0.43	1.47	1.72	1.68
31.6	20.6	-6.12	26.6	160.77	2.82	0.43	1.42	1.69	1.65
32.2	19.9	-6.13	26.8	161.8	2.84	0.43	1.44	1.72	1.68
33	18.9	-5.9	28	94.85	2.92	0.43	1.38	1.6	1.56
33.8	18	-5.91	28.8	95.78	2.96	0.43	1.38	1.63	1.59
34.5	17.3	-5.91	29.7	94.79	3.02	0.43	1.35	1.62	1.58
35.2	16.6	-5.83	30.9	72.76	3.08	0.44	1.3	1.54	1.49
36	15.9	-6.04	32.1	101.53	3.15	0.44	1.26	1.48	1.44
37	15	-6.03	32.9	90.6	3.2	0.44	1.26	1.52	1.47
38	14.3	-6.12	33.9	105.48	3.25	0.44	1.26	1.52	1.47

Table E.2. Atmosphere/wind fundamental properties for each model in the metallicity sequence for a fixed $T_\star = 16.1$ kK.

Z/Z_\odot	$\log \dot{M}$ [M_\odot yr $^{-1}$]	T_{23} [kK]	R_t [R_\odot]	$\log g$ [cm s $^{-2}$]	$\Gamma_e(R_{\text{crit}})$ [R_\star]	$R_{2/3}$ [R_\star]	R_{crit} [R_\star]	R_{sonic} [R_\star]
1.0	-5.30	9.1	57.3	0.96	0.41	3.15	8.55	4.88
0.8	-5.32	9.0	58.1	0.94	0.41	3.2	9.21	5.12
0.7	-6.54	10.0	435.4	1.13	0.42	2.59	11.42	7.64
0.6	-6.55	10.0	441.3	1.12	0.41	2.61	11.44	7.64
0.5	-6.64	10.1	522.3	1.14	0.42	2.54	10.57	7.28
0.4	-6.91	10.8	1067.6	1.26	0.42	2.21	6.10	4.98
0.3	-6.93	11.3	1261.3	1.34	0.42	2.02	4.37	3.83
0.2	-7.06	11.3	1562.6	1.34	0.42	2.02	4.62	4.01

Table F.1. Literature properties and updated distances and luminosities of LBVs and OBA hypergiants.

Star SIMBAD	Type	T_{eff} [kK] (lit.)	$\log L/L_{\odot}$ (lit.)	d_{pc} (lit.)	$\log L/L_{\odot}$ (new)	d_{pc} (lit.)	Ref. d_{pc} (new)	Ref. (lit.)
HR Car	LBV	17.9	5.69	5000	5.63	4677	BJ21	Gr09
		21.4	5.9	5000	5.84	4677	BJ21	vG01
MWC 930	LBV	22	5.5	3500	6.18	7640	BJ21	Mi14
		8	5.5	3500	6.18	7640	BJ21	Mi14
HD160529	LBV	10	5.46	2500	5.16	1769	BJ21	vG01
		7.8	5.46	2500	5.16	1769	BJ21	St91
HD316285	LBV	10.1	5.44	1850	5.84	2943	BJ21	Hi98
		11.7	6.17	10000	6.17	10000	Ue01	Cl09a
AFGL2298	LBV	10.9	6.11	10000	6.11	10000	BJ21	Cl09a
		10.3	6.3	10000	6.30	10000	BJ21	Cl09a
		10.9	6.17	10000	6.17	10000	BJ21	Cl09a
		13.2	5.75	6000	5.44	4203	BJ21	Cl09b
[OMN2000] LS1	LBV	13.4	5.3	3400	5.48	4203	BJ21	Cl09b
		13.7	4.86	2000	5.51	4203	BJ21	Cl09b
		19	5.86	4500	5.81	4230	Ne22	C-N04
W243	LBV	8.5	5.86	4500	5.81	4230	BJ21	Ri09
P Cyg	LBV	18.7	5.78	1610	5.76	1574	BJ21	Rv20
HD183143	BHG	12.8	5.46	2200	5.45	2187	BJ21	WB22
HD168625	BHG	14	5.58	2800	5.01	1452	BJ21	Ma16
HD168607	BHG	8.5	5.31	2200	5.09	1706	BJ21	Ch89
zet1 Sco	BHG	17.2	5.93	1640	6.03	1845	BJ21	Cl12, MBP25
HD199478	BHG	12.7	5.46	2400	5.48	2444	BJ21	WB23
Schulte 12	BHG	13.7	6.28	1750	6.21	1610	BJ21	Cl12
BP Cru	BHG	18.1	5.67	3040	5.81	3575	BJ21	Cl12
HD190603	BHG	18	5.58	1570	5.75	1918	BJ21	Cl12
HD80077	BHG	17.7	6.53	3600	6.26	2626	BJ21	Ha18
MWC 349A	LBV	25	5.75	1400	5.85	1563	BJ21	G-M12
MWC 314	LBV	18	5.85	3000	6.06	3821	BJ21	Lo13
GAL 024.73+00.69	LBV	12	5.6	5200	5.26	3500	Pe12	Cl03
Sher 25	BSG	20.9	5.48	5740	5.50	5857	BJ21	WB23
AG Car	LBV	22.8	6.17	6000	6.02	5039	BJ21	Gr09, Gr11
		22.8	6.17	6000	6.02	5039	BJ21	Gr09, Gr11
		21.5	6.17	6000	6.02	5039	BJ21	Gr09, Gr11
		17	6.17	6000	6.02	5039	BJ21	Gr09, Gr11
		16.4	6	6000	5.85	5039	BJ21	Gr09, Gr11
		14	6	6000	5.85	5039	BJ21	Gr09, Gr11
		14.3	6.04	6000	5.89	5039	BJ21	Gr09, Gr1
[GKF2010]MN 112	LBV	17.4	6.14	13560	6.14	13560	BJ21	Mv22
HD169454	BHG	20.4	5.92	1540	6.12	1944	BJ21	RD22, Na95
qF 362	LBV	11.3	6.24	8000	6.26	8230	Le22	Na09
Pistol Star	LBV	11.8	6.2	8000	6.22	8230	Le22	Na09
GRS 79.29+0.46	LBV	20.4	5.4	1700	5.54	2000	Hi94	Ag14
WRAY 17-96	LBV	20	6.47	4500	6.45	4383	BJ21	Eg02
Peony Star	WNL	25	6.5	8000	6.52	8230	Le22	Ba08
eta Car	LBV	9.4	6.69	2000	6.85	2400	Hu23	Gr12
Hen 3-519	LBV	15.1	6.26	8000	6.19	7342	BJ21	S-S17, vG01
[GKF2010] MN48	LBV	14	5.5	4000	5.58	4369	BJ21	Kn16
AS 314	PAGB	9.5	3.65	1614	3.65	1614	BJ21	Bh25
WRAY 16-232	LBV	12.5	5.7	2100	5.75	2226	BJ21	Ar25
GAL 026.47+00.02	LBV	17	6	6500	5.97	6267	BJ21	Cl03
GCIRS 16NE	WNL	24.1	6.34	8500	6.31	8230	Le22	Nz12, Na97
GCIRS 16C	WNL	19.5	5.9	7600	5.97	8230	Le22	Ma07
GCIRS 33SE	WNL	18	5.75	7600	5.82	8230	Le22	Nz12
GCIRS 16SW	WNL	24.4	6.41	8500	6.38	8230	Le22	Na97
WRAY 15-751	LBV	30	5.91	6000	6.10	7444	BJ21	Nz12, Pa06, vG01
GCIRS 34W	WNL	19.5	5.5	7600	5.57	8230	Le22	Ma07
GS Mus	OHG	28	5.28	2784	5.28	2784	BJ21	This work
HD151804	OHG	28.2	6.18	2140	6.18	2140	BJ21	This work

Notes. Gr09: Groh et al. (2009), vG01: van Genderen (2001), Mi14: Miroshnichenko et al. (2014), St91: Sterken et al. (1991), Hi98: Hillier et al. (1998), Cl09a: Clark et al. (2009b), Cl09b: Clark et al. (2009a), C-N04: Clark & Negueruela (2004), Ne22: Negueruela et al. (2022), Ri09: Ritchie et al. (2009), Rv20: Rivet et al. (2020), WB22: Weßmayer et al. (2022), Ma16: Mahy et al. (2016), Ch89: Chentsov & Luud (1989), Cl12: Clark et al. (2012), BP25: Bernini-Peron et al. (2025), WB23: Weßmayer et al. (2023), Ha18: Haucke et al. (2018), G-M12: Gvaramadze & Menten (2012), Lo13: Lobel et al. (2013), Cl03: Clark et al. (2003), WB23: Weßmayer et al. (2023), Gr11: Groh et al. (2011), Mv22: Maryeva et al. (2022), RD22: Rubio-Díez et al. (2022), Na95: Najarro (1995), Na09: Najarro et al. (2009), Ag14: Agliozzo et al. (2014), Eg02: Egan et al. (2002), Ba08: Barniske et al. (2008), Gr12: Groh et al. (2012), S-S17: Smith & Stassun (2017), Kn16: Kniazev et al. (2016), Bh25: Bakhytkyzy et al. (2025), Ar25: Arun et al. (2025), Nz12: Nazé et al. (2012), Ma07: Martins et al. (2007), Na97: Najarro et al. (1997), Ue01: Ueta et al. (2001). Pa06: Pasquali et al. (2006), Sm06: Smith (2006), Hu23: Hur et al. (2023), Le22: Leung et al. (2023), Pe12: Petriella et al. (2012)